# Multiscale characterization of effective mechanical properties of graphene-chitosan composite aerogels

D.-T. Le, V.-H. Nguyen, Samia Mahouche-Chergui, Benjamin Carbonnier, Daniel Grande, Salah Naili

# Multiscale characterization of effective mechanical properties of graphene-chitosan composite aerogels

D.-T. Le[a,b], V.-H. Nguyen[a], S. Mahouche-Chergui[b], B. Carbonnier[b], D. Grande[b,c], S. Naili[a,*]

[a] *Univ Paris Est Creteil, Univ Gustave Eiffel, CNRS, UMR 8208, MSME, F-94010 Créteil, France*
[b] *Univ Paris Est Creteil, CNRS, ICMPE, UMR 7182, 2 rue Henri Dunant, 94320 Thiais, France*
[c] *Present address: Univeristy of Strasbourg, CNRS, ICS, UPR 22, 23 rue du Loess, 67034 Strasbourg, France*

**Abstract**

This work reports on numerical characterizations of effective mechanical properties associated with graphene-polymer composite aerogels produced using an environmentally friendly freeze-drying process. To this purpose, a multiscale approach was implemented, in which geometrical configurations were constructed based on the results of experimental characterizations. A homogenization procedure based on molecular mechanics, the Milton method, and the asymptotic homogenization method was applied. In the asymptotic homogenization method, cell problems were formulated and solved within a representative volume element using the finite element method. After validating the numerical model through experimental results from compression tests, a parametric study on the influence of microstructural parameters of the materials, such as dispersion state, aspect ratio, volume fraction of nanoinclusions, and material porosity, on the macroscopic mechanical behaviour of the composite aerogels was conducted. The simulation results provided a deeper understanding of the mechanisms that enhanced the mechanical properties of such aerogels by adding various graphene derivatives, allowing for adjustments in the elaboration process to obtain materials with improved mechanical properties.

*Keywords:* Asymptotic homogenization, effective mechanical properties, finite element method, composite aerogel, graphene, biopolymer

**Materials Today Communications, 40 (2024) 109491**

## 1. Introduction

Aerogels constitute a unique class of ultralight porous materials. Despite their name, aerogels are solid, elastic, and dry materials that do not resemble a gel in their physical properties. The name comes from the fact that they are made from gels. In particular, the result is a solid with extremely low density and extremely low thermal conductivity. With their outstanding thermal insulation performance, aerogels have garnered significant attention in the building sector in recent years as a potential replacement for traditional insulation materials [1, 2]. In 2020, it is noteworthy that biomedical applications of these hybrid aerogels were reviewed and discussed [3]. While most aerogels are traditionally produced from high-cost and environmentally unfriendly materials, such as silica or synthetic polymers, the use of biopolymers in combination with eco-friendly freeze-drying methods offers a sustainable alternative [4, 5, 6]. It is noteworthy that chitosan (CS), one of the most common biopolymers, is a promising candidate due to its biocompatibility, biodegradability, and versatility [7]. The commonly used supercritical $CO_2$ drying method requires large amounts of solvents as well as expensive $CO_2$ extraction, leading to increased costs and possible adverse environmental impacts in the production process [8]. In contrast, the freeze-drying method has great advantages thanks to the direct use of water as the solvent and the simple drying process through its sublimation [9].

To be applicable in practical applications, aerogels need to exhibit favorable mechanical properties to withstand physical forces during usage and ensure their reusability. Graphene (G) and its derivatives, with excellent stiffness, have recently been used to enhance the mechanical strength of biopolymer-based aerogels [10, 11]. These experimental works all showed that the addition of graphene to a polymer matrix improved the mechanical properties of the aerogel.

*Corresponding author
*Email address:* naili@u-pec.fr (S. Naili)

However, to gain a deeper understanding of how graphene enhances the mechanical properties of aerogels, experimental approaches face challenges due to the need for precise control over the dispersion of graphene sheets during the aerogel elaboration. Therefore, it is necessary to use models not only to predict the effective mechanical properties of aerogels but also to guide the material elaboration stage. In the literature, analytical methods such as Mori-Tanaka [12, 13] and Halpin-Tsai [14, 15] are widely used to evaluate the effective properties of two-phase materials. Although these analytical methods require a low computational cost with reasonable accuracy, they cannot accurately account for interactions between adjacent inclusions and cannot describe local stress and strain effects [15, 16]. Conversely, the asymptotic homogenization method combined with the finite element method (FEM) can be a relevant choice to determine the effective properties of the aerogel due to its complex morphology. The asymptotic homogenization method is based on the representation at the microscale of a periodic unit cell of the material to describe its mechanical behavior at the macroscale. These methods have been successfully developed and used to obtain the effective mechanical properties of multifunctional materials as polymer/clay nanocomposites [17, 18].

It has been demonstrated that the arrangement and aspect ratio of the graphene sheets are important factors affecting the mechanical properties of polymer-based composites [19, 20]. However, to the best of our knowledge, no studies have explored the influence of these microscale factors on the mechanical properties of aerogels, in which factors beyond pore shape and porosity may also be affected. Furthermore, graphene oxide (GO), a derivative of graphene, is commonly used to enhance the mechanical strength of polymer-based aerogels due to its excellent dispersibility. Nevertheless, there have been no studies specifically comparing the mechanical strengthening ability between these two types of nanomaterials to address the question of whether the effort to oxidize graphene sheets to form graphene oxide is reasonable.

The main objective of this study is to conduct a comprehensive characterization of the effective mechanical properties of graphene-chitosan binary hybrid aerogels specially elaborated. To accurately estimate the effective mechanical properties of the aerogels under investigation, we have adopted a multiscale approach in which geometrical configurations are constructed based on the findings from experimental characterization. This investigation aims to provide valuable insights into the pivotal role of graphene in augmenting the mechanical performance of the aerogels. Additionally, it seeks to compare the mechanical reinforcement capabilities of both graphene and graphene oxide under specific scenarios.

As a consequence, our contribution in the present paper is the following:

1. Purposefully elaborated chitosan aerogels with diverse graphene contents were systematically characterized for their structural, morphological, and mechanical features, providing crucial inputs for developing a robust numerical model.

2. To the best of our knowledge, it is the first attempt that a multiscale characterization of the effective mechanical properties of graphene/polymer-based hybrid aerogels is carried out.

3. We conducted extensive studies on the effect of the microstructural morphology, such as aggregate, intercalated and exfoliated structures, on the effective mechanical properties of these aerogels.

To characterize the hybrid aerogels, a multiscale approach was applied in which geometrical configurations were built at three levels based on experimental results. The nanoscale included multilayered graphene and graphene oxide blocks; the microscale was the solid phase of the aerogels consisting of randomly arranged graphene and graphene oxide blocks within a polymer matrix; finally, the macroscale described the porous solid framework structure of the aerogels. The effective mechanical properties of the material were determined using analytical methods, including molecular mechanics and the Milton method at the nanoscale, as well as the asymptotic homogenization approach at the micro and macro scales.

The paper is organized as follows. Section 2 introduces the elaboration method and experimental characterization of the graphene-chitosan aerogels under investigation. Subsequently, sections 3 and 4 present the construction of geometrical configurations and homogenization methods at different scales, respectively. The numerical results and a discussion about the mechanical properties are reported in section 5. In the latter, the obtained numerical results are also compared with our experimental results and those of previous experimental work in the literature. Finally, section 6 summarizes the main conclusions of this work. Kelvin notation used in this work is presented in Appendix A.

## 2. Material elaboration and characterization

### *2.1. Elaboration method*

The aerogels made of chitosan (CS) and graphene (G) were synthesized through an environmentally friendly freeze-drying process. The aerogels were formed by freezing the precursors mixed in an aqueous medium, and then dried by replacing the liquid phase with a gas phase to form an aerogel, which was the basis of the aerogel synthesis process. In order to prevent the skeleton from collapsing during the drying process, freeze-drying permitted to convert water from the solid phase to a gas phase (sublimation) in a low pressure environment while keeping the shape of the skeleton intact [21]. Accordingly, the wet gel was initially frozen and then subjected to low-temperature and low-pressure conditions for sublimation. The $G_x$-CS hybrid aerogels synthesis, where $x$ is the mass percent of graphene in CS, was performed based on previously reported methods [11] as shown in Fig. 1. Typically, the chitosan solution (24 mg/mL) was prepared by dissolving 2.4 g of chitosan powder in 100 mL of acetic acid aqueous solution (1% v/v). Then, the homogeneous graphene suspension with different amounts of graphene nanoinclusions ($x$% weight ratio with respect to the amount of chitosan) prepared through ultrasonic treatment was added to the chitosan solution. The resulting mixture was then poured into molds and pre-frozen at −60 ℃ for 24 h in a temperature-controlled freezer. Finally, the sample was completely dried by freeze-drying after 48 h.

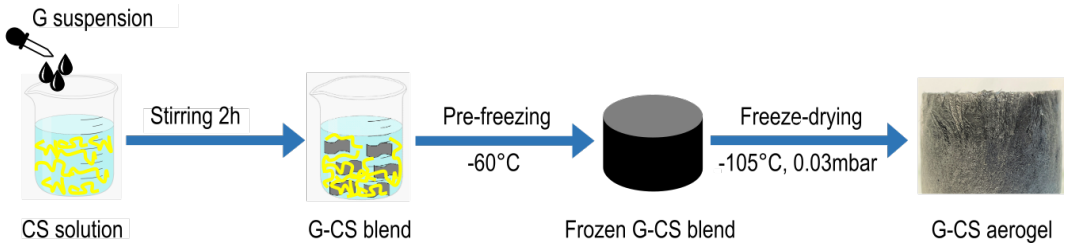


Figure 1: Schematic diagram of the graphene-chitosan hybrid aerogel fabrication using the freeze-drying method.

### *2.2. Experimental characterization*

The multiscale structure and morphology of graphene-chitosan aerogels were studied by X-ray diffraction analysis (XRD), transmission electron microscopy (TEM), and scanning electron microscopy (SEM). XRD analysis gave insight about the distribution of graphene sheets in the chitosan matrix. According to the XRD results (see Fig. 2(a)), the graphene sheets in the original graphene powder had a typical XRD diffraction peak at 26.6° that corresponded to an interlayer spacing of 0.335 nm. The characteristic peaks for chitosan crystalline structure were observed at $2\theta$ equal to 10° and 20° in chitosan powder, respectively. In G-CS aerogel, two broad peaks at 8.9° and 19.2° were observed. Additionally, a weak peak at 26.3° was also found, indicating the presence of graphene with an interlayer distance of 0.338 nm. The graphene layer distance was almost constant indicating that the intercalated and exfoliated structures were not achieved.

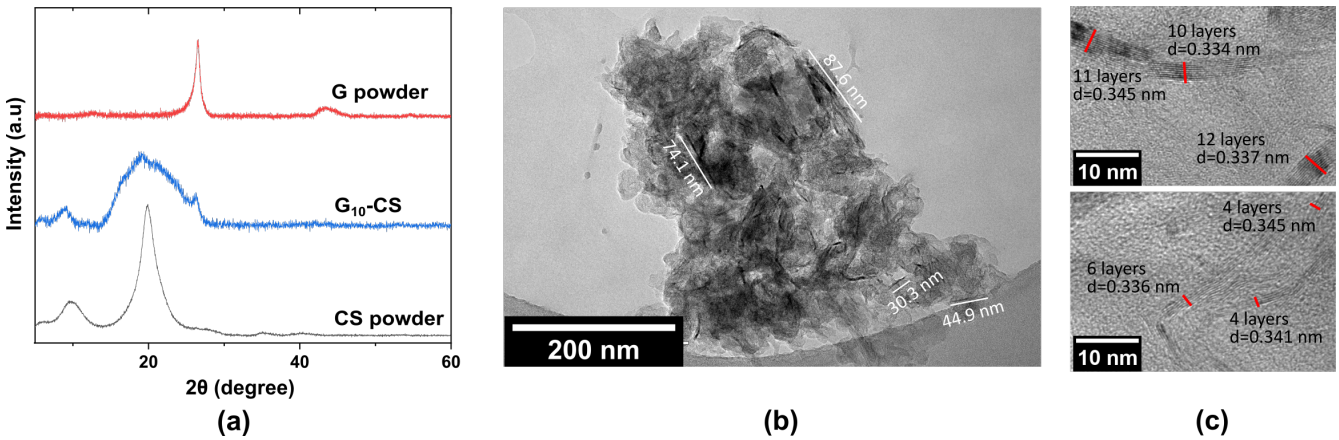


Figure 2: (a) XRD patterns of graphene powder, $G_{10}$-CS aerogel and chitosan powder, (b) low-resolution TEM image and (c) high-resolution TEM image of $G_{10}$-CS aerogel.

To better characterize the structure of graphene in the G-CS aerogels, TEM analysis was conducted for the $G_{10}$-CS sample, as shown in Fig. 2(b)-(c). From these figures, it could be observed that graphene sheets formed aggregates where they were arranged parallel to each other. There were $4-12$ layers in each aggregate with interlayer spacing ranging between 0.334 and 0.345 nm, which coincided with the results obtained from the XRD analysis above. In addition, these aggregates were randomly distributed in the chitosan matrix with a length varying from $30.3 - 87.6$ nm.

Unlike graphene, graphene oxide (GO) was easily dispersed in the polymer matrix to form intercalated or exfoliated structures thanks to its surface functionality [22]. The efficiency of dispersion, which was related to the amount of intercalation based on the graphene oxide interlayer spacing (which is infinity for the exfoliated structure), depended on the type of polymer present and the graphene oxide content relative to the polymer [23]. In the work of Blanton *et al.* [23], the distance between two graphene oxide sheets in composites with various polymers and different polymer content were valid in the range of $1.5 - 5.3$ nm. Therefore, two types of structures (intercalated and exfoliated) of graphene oxide were also considered to compare its ability to enhance mechanical properties with that of graphene.

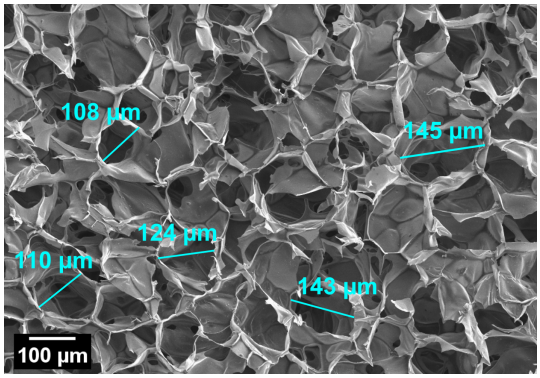


Figure 3: SEM micrograph of G(10 %)-CS aerogel.

Pore features were preliminary characterized by SEM analysis. The SEM images were processed in the *ImageJ* software to determine pore sizes. The number of pores to be evaluated was 30 where evaluation was performed twice in two perpendicular directions for each pore. According to the SEM micrographs (see Fig. 3), a three-dimensional structure consisting of a network of thin alveolus could be found. The alveolus forms an interconnected pores network with the average diameter of 76 $\mu$m. The interconnection of pores was characterized by a void with an average diameter of 12 $\mu$m. This result was consistent with the aerogel structure synthesized by the freeze-drying method in previous studies [10, 11].

## 3. Multiscale geometrical configuration and materials properties

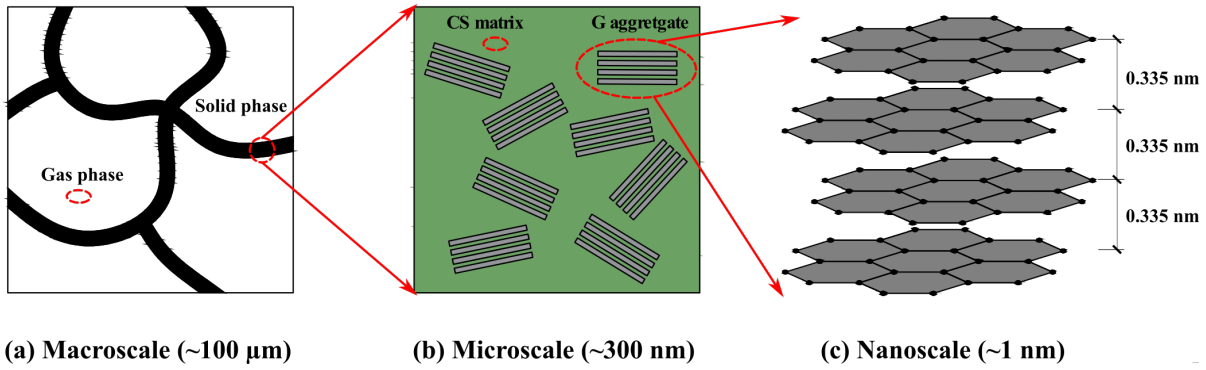


Figure 4: Schematic illustration of the multiscale structure of graphene-chitosan composite aerogels including (a) macroscale depicting solid and gas phases, (b) microscale depicting the distribution of graphene blocks in chitosan matrix and (c) nanoscale describing the graphene sheets in graphene block.

Based on the experimental results presented in the previous section, the multiscale structure of the graphene-chitosan composite aerogels was divided into three separate scales. The first scale (scale qualified of nanoscale) was the aggregation of graphene sheets (named graphene blocks) consisting of many parallel graphene sheets, the second one was the microscale where the graphene blocks dispersed in the chitosan matrix to form the solid phase of the aerogels, and finally, the macroscale was made of gas phase and solid phase as shown in Fig. 4. In this section, the geometrical configurations at different scales are presented and discussed as the material properties of the constituents.

### *3.1. Geometrical configuration at the nanoscale*

As demonstrated by XRD and TEM analyses, the graphene block consists of graphene sheets arranged parallel to each other with a distance between two sheets of 0.335 nm and the number of graphene layers is in the range of $4 - 12$ layers (see Fig. 5(a)). The aggregation of graphene sheets was caused by van der Waals interactions, so the structure of the graphene block resembled that of crystalline graphite [24]. Therefore, the geometrical configuration of the graphene block consisted of parallel two-dimensional graphene sheets with a distance between two sheets of 0.335 nm which interacted with each other by van der Waals forces. Each graphene sheet was composed of a hexagonal lattice of carbon atoms.

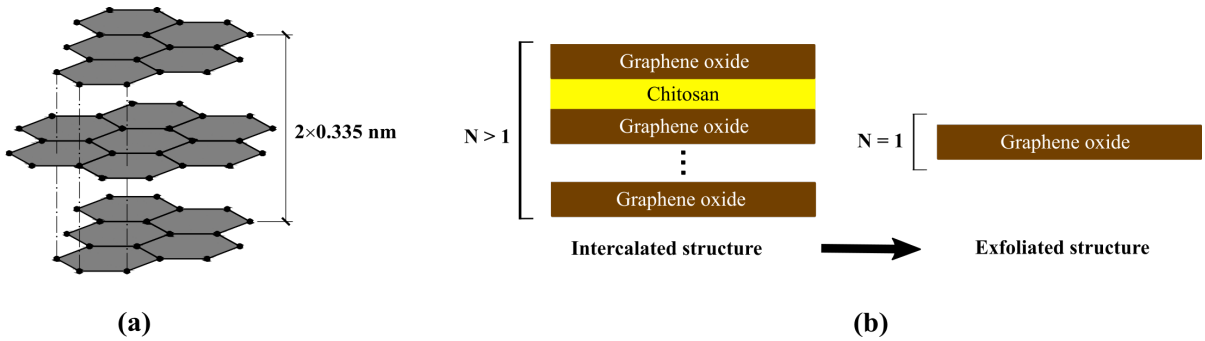


Figure 5: Description of three geometrical configurations at the nanoscale including (a) the aggregate structure of graphene corresponding to graphene block and (b) the intercalated and exfoliated structure of graphene oxide corresponding to graphene oxide block and monolayer graphene oxide, respectively.

Even if graphene oxide is known for its ability to readily disperse in polymer to form an exfoliated structure as discussed in section 2, in practice, one obtained an intercalated structure in some cases. Therefore, the intercalated and exfoliated structures were considered for the graphene oxide-chitosan hybrid aerogel (see Fig. 5(b)). The number of graphene oxide layers per block, denoted by $N$, was greater than 1 for the intercalated structure and equal to 1 for the exfoliated structure. In the intercalated structure, since the distance between the two graphene oxide layers was in the range of $1.5 - 5.3$ nm [23] and the thickness of graphene oxide was approximately 1 nm, which was experimentally measured in many previous reports [25, 26], the thickness of the polymer (chitosan) intercalated between the graphene oxide layers was taken to be equal to 2 nm.

### *3.2. Geometrical configuration at the microscale*

In previous works [27, 28], the shape of graphene and graphene oxide was considered to be that of a disc of circular cross-section. Therefore, each graphene block and graphene oxide block was also included in the geometrical configuration as disc-shaped.

With the results from the TEM image in section 2.2, the graphene blocks had a length of $30.3 - 87.6$ nm and a thickness of $1.36 - 4.04$ nm. The aspect ratio $r_a$ of the graphene blocks, defined by the ratio between diameter $d_m$ and thickness $h_m$, could be estimated in the range of $8 - 65$. This result was consistent with the aspect ratio of graphene aggregates measured in previous works [29, 30]. It could be noted that this aspect ratio was not too large. The decrease in aspect ratio could be explained by the dispersion of graphene through ultrasonic treatment [30]. In the present work, the aspect ratio was taken into account in the model to investigate the effect of this parameter on the entire aerogel behavior. It is noteworthy that in many studies, the typical values of the aspect ratio and the number of graphene layers of the block were taken as 40 and 5 respectively. Besides, since the graphene blocks had a random orientation in the chitosan matrix, the inclusions which represented the graphene blocks in the chitosan matrix, were therefore modeled by discs of arbitrary orientation and position in the chitosan matrix.

Just like graphene, the graphene oxide monolayer had an aspect ratio that varies from 10 [31] up to more than 1000 [26], depending on the graphene oxide preparation method or the graphene oxide dispersion method in the

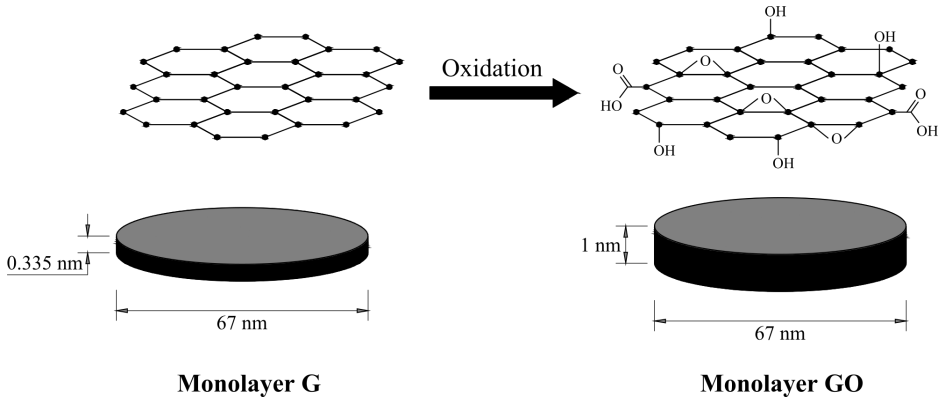


Figure 6: Illustration of the oxidation of graphene to graphene oxide with the lateral dimension unchanged at the nanoscale.

polymer matrix. In order to compare the influence of the graphene oxide *versus* graphene on the material properties of the aerogels, we assumed that the diameter of the monolayer graphene oxide was taken to be equal to the diameter of the graphene monolayer. For example, with a typical graphene block having an aspect ratio of 40 and 5 graphene layers, the size of the monolayer graphene sheet in this block was evaluated to be equal to 0.335 nm and 67 nm for thickness and diameter, respectively. Therefore, the diameter of the monolayer of graphene oxide sheet was also taken to be equal to 67 nm. With a thickness of 1 nm, the aspect ratio of graphene oxide monolayer was equal to 67 (see Fig. 6). For the intercalated structure of graphene oxide, the number of graphene oxide layers per block was also taken to be equal to 5, as for graphene block. In addition, the graphene oxide monolayer or graphene oxide blocks were arranged with arbitrary orientations in the chitosan matrix as in the case of graphene.

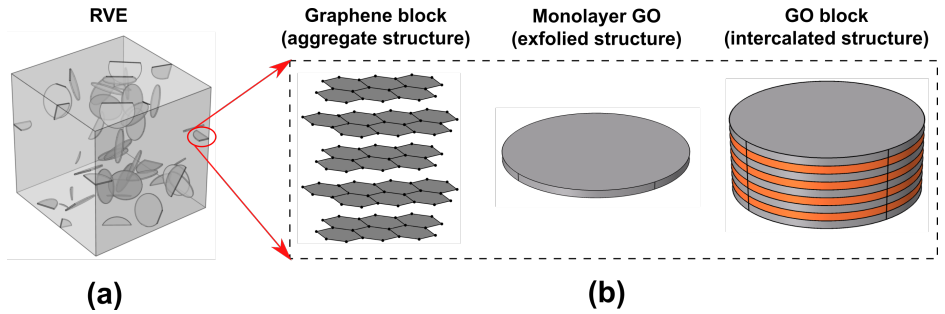


Figure 7: Description of (a) representative volume element at the microscale for 1% concentration by volume of randomly oriented inclusions and (b) three types of inclusions: graphene block, graphene oxide monolayer and graphene oxide block.

Collectively, the representative volume element (RVE) at the microscale consisted of disc-shaped inclusions randomly distributed in the chitosan matrix. Inclusions could be one of three forms: graphene block, monolayer graphene oxide and graphene oxide block (see Fig. 7).

### *3.3. Geometrical configuration at the macroscale*

The cell periodicity feature facilitated the evaluation of average properties. It was based on the idea of a representative volume element (RVE). The RVE was a domain representative for the material on a microscopic scale. A RVE was typically identified as the smallest possible unit cell of a material. The RVE shape was required to possibly fill space with a repetitive pattern of RVEs. This meant that there were a set of matching boundary pairs, each of them having the same geometry, but offset by a given distance. To construct this unit cell, the factors to be included were pore shape, pore size, connected hole size, and porosity. The unit cell must represent the material properties of the entire material. In the literature, two main morphologies of aerogels were considered leading to an anisotropic or isotropic behavior of the structure which was obtained by using different freezing methods depending on the use of the aerogels. For the anisotropic structure, two controlled freezing methods were used: unidirectional freezing giving rise to a structure with tubular pores parallel to the freezing direction [10] and bidirectional freezing giving rise to a structure with parallel layer lamellars [32]. For the isotropic structure, the aerogels were frozen by ensuring freezing and freezing rates in all directions. This freezing method used in our work resulted in the generation of cellular structure with an interconnected pores network whose average pore diameter

was equal to 76 $\mu$m. This result was consistent with previous works using the same freezing method, where the pore size range varied from a few tens of micrometers to several hundreds of micrometers [11, 10]. Therefore, the unit cell representing the macrostructure of the material was a hollow sphere with a diameter of 76 $\mu$m as shown in Fig. 8. Six holes with a diameter of 12 $\mu$m were made on the wall of the hollow sphere to create the interconnected pores network among the unit cells.

It is noteworthy that the RVE geometry at the macroscale was defined based on the geometry of the matrix and pore phases, both of which were assumed to be purely elastic. The geometry of matrix phase is shown in Fig. 8(c). The geometry of the pore phase was the cube containing the matrix phase, with the latter being subtracted. Figure 9 shows the geometry of the representative unit cell at the macroscale with the matrix (green) and pore (grey) phases. Moreover, since elasticity moduli of the pore phase were equal to zero, this property was used to simplify the equation system to solve (see section 4.3.3).

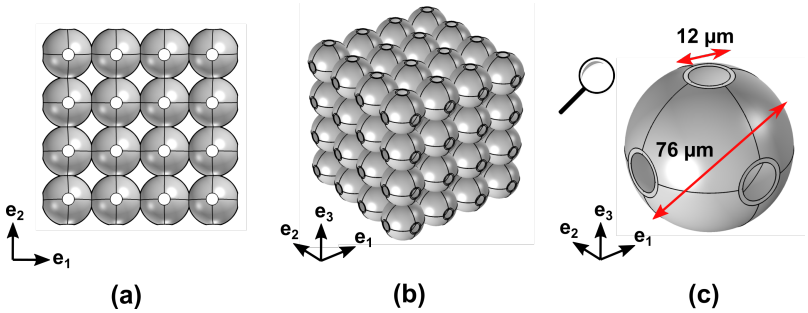


Figure 8: (a) The vertical view of the geometrical configuration at the macroscale; (b) the tridimensional view of the overall geometrical configuration as an array consisting of periodic unit cells along the $\mathbf{e}_1$, $\mathbf{e}_2$, and $\mathbf{e}_3$ -directions; and (c) the representative unit cell at the macroscale.

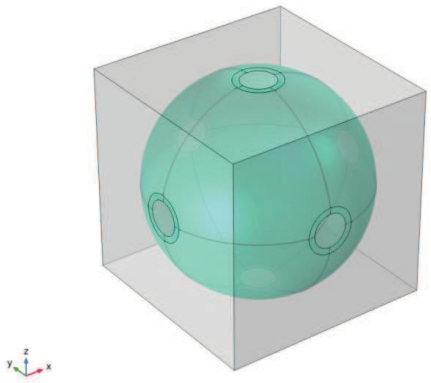

Figure 9: Geometry of the representative unit cell at the macroscale with the matrix (green) and pore (grey) phases.

In addition to the diameters of the hollow sphere and the holes in the wall, in order to fully characterize the unit cell, the wall thickness of the hollow sphere must be defined. This thickness was defined by introducing the porosity of the unit cell which was the volume fraction of gas phase in the unit cell. Due to the periodicity, the porosity of aerogel was calculated through the relationship between aerogel porosity and aerogel density. This relationship is expressed by the following relationship:

$$\phi_a = 1 - \frac{\rho_a}{\rho_s}, \tag{1}$$

where $\phi_a$ and $\rho_a$ are the porosity and the apparent mass density of aerogel, respectively. The quantity $\rho_s$ was the mass density of the solid phase related to the mass density of the graphene $\rho_G$ and chitosan $\rho_{CS}$ components according to the following relationship:

$$\rho_s = \frac{(f_w + 1)\rho_G\, \rho_{CS}}{f_w\, \rho_{CS} + \rho_G}, \tag{2}$$

where $f_w$ is the graphene weight fraction relative to chitosan. In the model, graphene was introduced by volume fraction $f_v$, where $f_v$ is defined as the ratio of the volume of graphene to the volume of the RVE. In the experiment, graphene was added to the polymer as a percentage by mass of polymer $f_w$. Therefore, for instance, the relation between $f_v$ and $f_w$ in aerogel is given by the relationship:

$$f_v = \frac{\rho_{CS} f_w}{\rho_{CS} f_w + \rho_G}. \tag{3}$$

Table 1: Apparent mass density and calculated porosity of aerogels.

| Graphene weight fraction $f_w$ (%) | Graphene volume fraction $f_v$ (%) | Apparent mass density $\rho_a$ (g/cm$^3$) | Porosity $\phi_a$ (%) |
|---|---|---|---|
| 0 | 0 | 0.0256 ± 0.0012 | 98.25 ± 0.08 |
| 2.5 | 1.59 | 0.0261 ± 0.0010 | 98.23 ± 0.07 |
| 5 | 3.13 | 0.0262 ± 0.0002 | 98.24 ± 0.01 |
| 7.5 | 4.62 | 0.0277 ± 0.0006 | 98.15 ± 0.04 |
| 10 | 6.06 | 0.0290 ± 0.0014 | 98.08 ± 0.09 |
| 15 | 8.83 | 0.0302 ± 0.0004 | 98.03 ± 0.03 |

For pure chitosan aerogel, the value of $\rho_{CS}$ was taken to be equal to 1.463 g/cm$^3$ based on literature data [33]. The mass density of graphene was taken to be equal to the mass density of crystalline graphite which was equal to $\rho_G = 2.267$ g/cm$^3$ [34]. Given the measured apparent mass densities of the aerogels, their overall porosity is shown in Tab. 1. It could be seen that with the graphene weight fraction below 5% (corresponding to the graphene volume fraction below 3.13%), the porosity of the aerogel did not change significantly (from 98.23 to 98.25%), which was consistent with previous works [10, 35]. Therefore, in the parametric study, the values of graphene volume fraction $f_v$ took their values in the range of $0 - 3\%$, and the value of aerogel porosity was taken with an average value of 98.24%. Besides, a study on the influence of porosity on the effective material properties of chitosan aerogel (corresponding to $f_v = 0$) was also carried out in the porosity range $86 - 99\%$.

### *3.4. Properties of the material's constituents at the nanoscale*

Graphene is a material well known for its outstanding mechanical strength. In the literature, the graphene sheet is assumed to behave like a linear isotropic material. The Young's modulus of graphene monolayer was measured by various methods. The value of Young's modulus of graphene monolayer experimentally measured was approximately equal to 1 TPa [36]. However, when graphene sheets were very close together by a weak van der Waals interactions forming blocks, the material properties of these multilayer blocks in the out-of-plane direction (the direction perpendicular to the sheets) are much weaker than those in the in-plane direction. The effective material properties of graphene blocks were calculated using molecular mechanics, which will be detailed in the following section. The graphene oxide monolayer was considered as an isotropic elastic material with Young's modulus $E_{GO} = 470$ GPa and a Poisson's ratio $\nu_{GO} = 0.197$ based on literature data [37].

Material properties of chitosan were defined from literature. The values of Young's modulus of chitosan varied from 0.3 to 2.7 GPa [38, 39, 40]. This value range was quite wide because many factors could affect the mechanical strength of chitosan films, such as chitosan molecular weight, degrees of deacetylation of chitosan or acid solvent. Therefore, two values of Young's modulus of chitosan, $E_{CS} = 0.35$ GPa and $E_{CS} = 2.5$ GPa, were used in our investigation, then the numerical results were compared with the experimental ones. The Poisson's ratio of chitosan $\nu_{CS}$ was taken to be equal to 0.4.

## 4. Homogenization method

In this section, the multiscale and homogenization methods are presented in order to determine the effective mechanical properties at each scale. A multiscale method was carried out from the smallest scale (nanoscale) to the largest (macroscale) one where the results obtained at the smaller scale were the input for the next scale. A flowchart depicting the multiscale method and homogenization method used at each scale is shown in Fig. 10. In the following section, the Cartesian reference system was used where the orthonormal basis was specified by $(\mathbf{e}_1, \mathbf{e}_2, \mathbf{e}_3)$ and the coordinates of a point were denoted by $\mathbf{x} = (x_1, x_2, x_3)$.

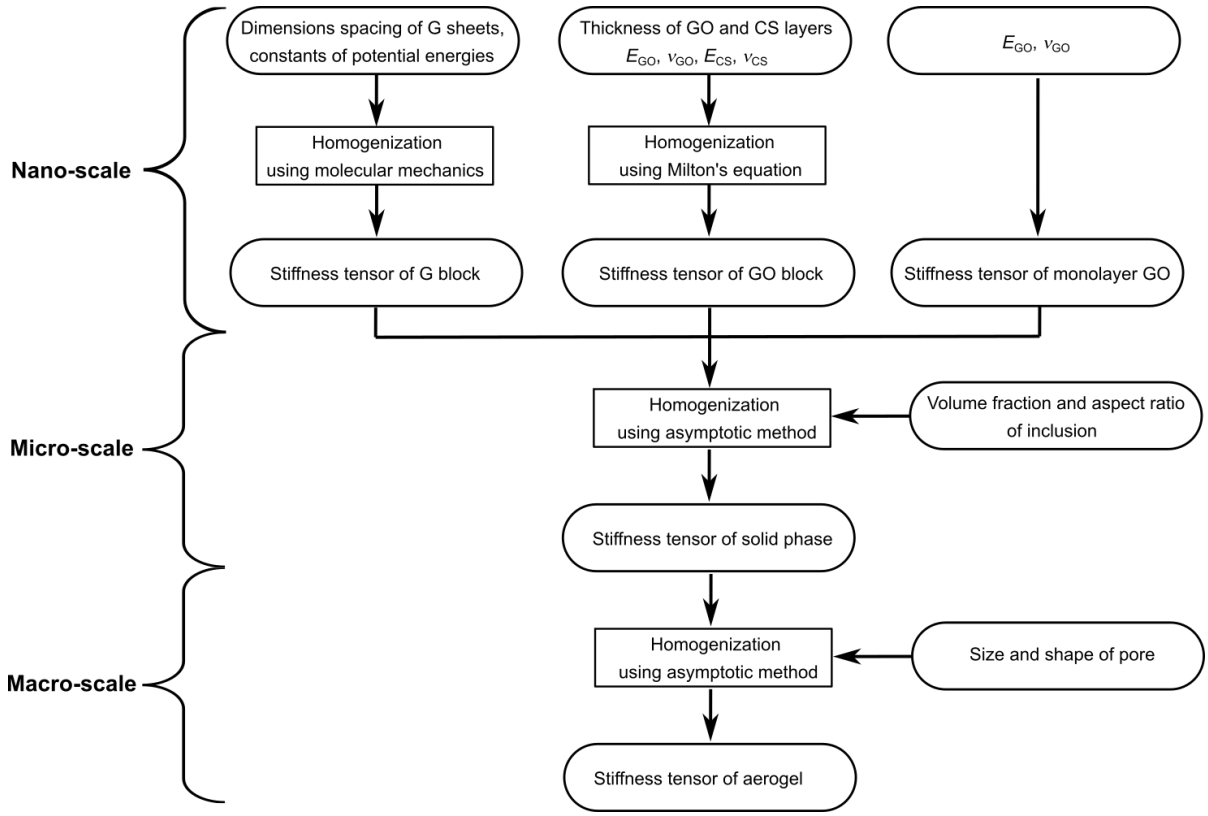


Figure 10: Flowchart of the multiscale method and homogenization method used at each scale to determine the effective mechanical properties of aerogels.

### *4.1. Determination of elastic properties of graphene block at the nanoscale*

In 2007, Cho *et al.* [13] reported in-plane and out-of-plane mechanical properties of graphite by using molecular mechanics. Because the structure of the graphene block was similar to that of graphite, we could follow the latter work [13] to calculate the effective material properties of the graphene block. For determining the material properties of out-of-plane graphite, Cho *et al.* [13] only used the interaction between two adjacent graphene sheets. Meanwhile, they used the model parameters issue from the work of Girifalco and Lad [41] which were deduced by considering the interaction between two semi-infinite graphite crystals. By comparison of the approach of Girifalco and Lad, Kelly and Duff [42] also gave parameter values by considering only the interaction between two adjacent graphene sheets and with known layer spacing. Therefore, in this section, we gave a general introduction to the principles of molecular mechanics and the main equations used in the work of Cho *et al.* [13] and simultaneously modify the constant when calculating the out-of-plane mechanical properties of the graphene block. Besides, we also extended to the arbitrary direction of block based on the work of Aboudi *et al.* [43].

#### *4.1.1. Structure of graphene block*

Like graphite, the graphene block has a layered structure consisting of many parallel layers of graphene, as shown in Fig. 11. The single layer of graphene is a hexagonal honeycomb lattice composed of tightly bound carbon atoms. The adjacent graphene layer, denoted as II in Fig. 11, is arranged by shifting it a length equal to $d$ of the layer denoted as I in Fig. 11 in the $\mathbf{e}_3$-direction, perpendicular to the plane, and translating it within its plane in the $\mathbf{e}_1$-direction by a distance equal to the side length of the hexagon, *i.e.* 1.42 Å [44].

In graphene, each carbon atom is covalently bonded to three other carbon atoms forming a bond angle of 120 °. With $sp^2$ hybridization, this covalent bond is even stronger than the $sp^3$ hybridized carbon-carbon bond in diamond [45]. In addition, interactions such as van der Waals ones, can occur not only between carbon atoms on the same sheet of graphene, but also between carbon atoms on a sheet and neighboring sheets. These interactions make the graphene sheets stable with interlayer spacing $d$ by the minimum energy assumption. In addition, van der Waals interactions are very weak compared to the covalent bond, resulting in graphene sheets being able to easily slide against each other. It can therefore be predicted that graphene block has a very high stiffness in the plane and a weaker stiffness in the out-of-plane direction.

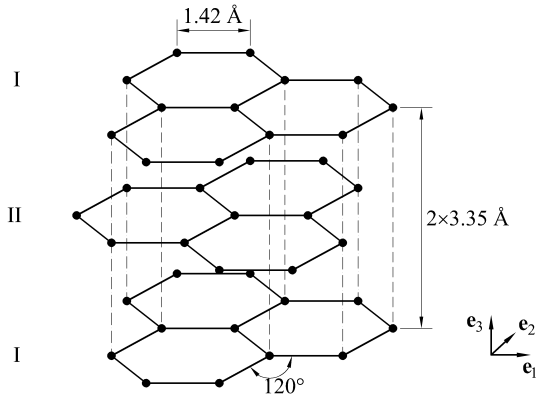


Figure 11: Geometrical configuration of graphene block structure.

*4.1.2. Interatomic potential functions in molecular mechanics*

Molecular mechanics uses classical mechanics to model systems at the molecular scale. This approach enables to investigate the mechanical behavior of systems at the molecular scale. It is intended to describe the change of the energy system according to the change of the position of each atom, then to give the relationship between the interacting forces and the position of each atom by derivation of the energy system. Finally, the mechanical behavior of the material is calculated from the stress-strain relationships. In molecular mechanics, the total potential energy $U_t$ can be expressed as a sum of several individual energy terms:

$$U_t = U_b + U_{ag} + U_{ts} + U_{iv} + U_{nb}, \tag{4}$$

where $U_b$, $U_{ag}$, $U_{ts}$ and $U_{iv}$ are potential energies associated with bond stretching, angle-bending, torsion and inversion, respectively. Potential energy $U_{nb}$ includes non-bonding energies typically due to the van der Waals and electrostatic interactions. A schematic illustration of each energy term is shown in Fig. 12.

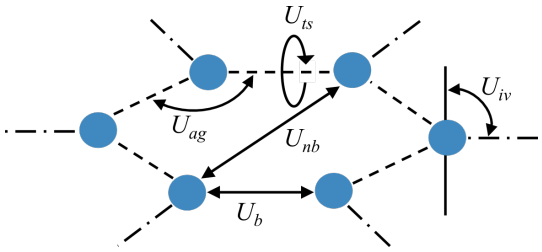


Figure 12: Bond structures and corresponding energy terms of a graphene cell (from [46]).

*4.1.3. In-plane elastic constants*

In-plane, the so-called engineering constants are the followings: $E_1^{gb}$, $E_2^{gb}$, $\mu_{12}^{gb}$, $\nu_{12}^{gb}$, $\nu_{21}^{gb}$, $\eta_{12,1}$, $\eta_{1,12}$, $\eta_{12,2}$ and $\eta_{2,12}$, where $E_1^{gb}$ and $E_2^{gb}$ are Young's *moduli* in tension-compression in the directions of the $\mathbf{e}_1$ and $\mathbf{e}_2$ axes respectively, $\mu_{12}^{gb}$ is the in-plane shear modulus, $\nu_{12}^{gb}$ and $\nu_{21}^{gb}$ are Poisson's ratios characterizing the contraction in the direction of one axis when tension is applied in the direction of another axis, $\eta_{1,12}$ and $\eta_{2,12}$ are coefficients of mutual influence of the first kind that characterizes stretching in the $\mathbf{e}_1$-direction caused by shear stress in the in-plane, $\eta_{12,1}$ and $\eta_{12,2}$ are coefficients of mutual influence of the second kind that characterizes in-plane stretching caused by normal stress in the $\mathbf{e}_1$ and $\mathbf{e}_1$ -directions respectively.

In this work, the coefficients of mutual influence were supposed negligible compared to other coefficients. Moreover, in accordance with the minor and major symmetric relationships of the elasticity tensor, the following relationships must be verified:

$$\frac{\nu_{12}^{gb}}{E_1^{gb}} = \frac{\nu_{21}^{gb}}{E_2^{gb}}. \tag{5}$$

Graphene block when subjected to in-plane loading denoted as $f$ (see Fig. 13(a)) at small strains, only bond stretching and angle-bending energy terms were significant in the total system potential energy. By using the

modified Morse potential function, total potential energy could be described as follows [13]:

$$U_t = U_b + U_{ag}, \tag{6}$$

$$U_b = \sum D\left[(1-\exp(-\beta\Delta r))^2 - 1\right], \tag{7}$$

$$U_{ag} = \frac{1}{2}\sum k_{\theta 1}(\Delta\theta)^2\left[1 + k_{\theta 2}(\Delta\theta)^4\right] \tag{8}$$

where $D = 6.031$ nNÅ, $\beta = 2.625$ Å$^{-1}$, $k_{\theta 1} = 14.2$ nNÅ/rad$^2$ and $k_{\theta 2} = 0.754$ rad$^{-4}$ [13]; $\Delta r$ and $\Delta\theta$ are the elongation of bond stretch and the variation of bond angle.

By taking the derivative of Eqs. (7) and (8) with respect to bond stretch and bond angle variation, one got the stretch force and the moment of the force about point $O$, respectively [13]:

$$F = 2\beta D\left(1-\exp(-\beta\Delta r)\right)\exp(-\beta\Delta r), \tag{9}$$

$$M(O) = k_{\theta 1}\Delta\theta + \text{ higher order terms of } \Delta\theta. \tag{10}$$

*Uniaxial tension in the* $\mathbf{e}_2$*-direction.* Applying a uniform load $f$ in the $\mathbf{e}_2$-direction (see Fig. 13(a)), based on the force and moment equilibrium equation of the bold part (left half) of stick $OA$ and the Eqs. (9)-(10), one obtained the relationship between $\Delta a$ and $\Delta\alpha_1$:

$$\Delta\alpha_1 = \frac{2a}{3}\frac{\beta D\left(1-\exp(-\beta\Delta a)\right)\exp(-\beta\Delta a)}{k_{\theta 1}}\cot(\frac{\alpha_1}{2}) \tag{11}$$

where $a = 1.42$ Å is the bond length of stick $OA$, $\Delta a$ is the variation of the bond length, $\alpha_1 = 2\pi/3$ is the bond angle and $\Delta\alpha_1$ is the angular variation of the bond.

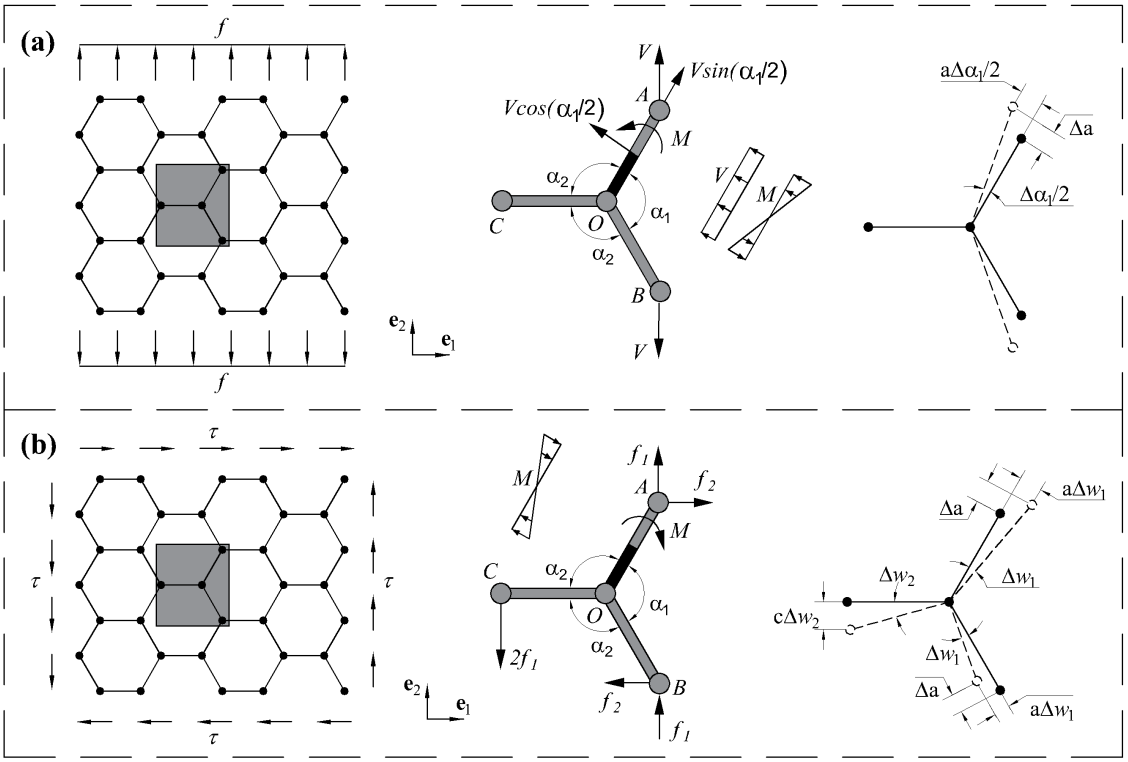


Figure 13: Schematic illustration of the loading of an infinite graphene sheet. The loading analysis of the representative cell and the deformation of the representative cell are decomposed (a) uniaxial tension in the $\mathbf{e}_2$-direction and (b) in-plane shear loading (based on [13]).

In-plane strains and axial stress in this case could be calculated from $\Delta a$ and $\Delta\alpha_1$ as follows:

$$\varepsilon_{11} = \frac{\Delta a \cos(\frac{\alpha_1}{2}) - \frac{a}{2}\Delta\alpha_1 \sin(\frac{\alpha_1}{2})}{a\left(1+\cos(\frac{\alpha_1}{2})\right)}, \tag{12}$$

$$\varepsilon_{22} = \frac{\Delta a \sin(\frac{\alpha_1}{2}) + \frac{a}{2}\Delta\alpha_1 \cos(\frac{\alpha_1}{2})}{a\sin(\frac{\alpha_1}{2})}, \tag{13}$$

$$\sigma_{22} = \frac{V}{a\left(1+\cos(\frac{\alpha_1}{2})\right)d} = \frac{2\beta D\left(1-\exp(-\beta\Delta a)\right)\exp(-\beta\Delta a)}{ad\left(1+\cos(\frac{\alpha_1}{2})\right)\sin(\frac{\alpha_1}{2})}. \tag{14}$$

The in-plane engineering constants of graphene block as defined by $E_2^{gb} = \sigma_{22}/\varepsilon_{22}$ and $\nu_{21}^{gb} = -\varepsilon_{11}/\varepsilon_{22}$ were determined by choosing the value of $\Delta a$ such that $\varepsilon_{22} = 0.1\%$.

Applying a uniform load $f$ in the $\mathbf{e}_1$-direction, a development analogous to the previous one led to the expressions of the in-plane strains and axial stress which permitted to define $E_1^{gb} = \sigma_{11}/\varepsilon_{11}$ and $\nu_{12}^{gb} = -\varepsilon_{22}/\varepsilon_{11}$.

*In-plane shear loading of a graphene sheet.* Similarly, when the graphene sheet was subjected to the shear loading $\tau$ in both directions (see Fig. 13(b)), the relationship between $\Delta a$ and $\Delta\alpha_2$ was given by:

$$\Delta\alpha_2 = \frac{a\beta D\left(1-\exp(-\beta\Delta a)\right)\exp(-\beta\Delta a)}{k_{\theta 1}} \frac{\sin(\frac{\alpha_1}{2})}{1+\cos(\frac{\alpha_1}{2})}, \tag{15}$$

where $\Delta\alpha_2 = \Delta w_1 + \Delta w_2$ with $-\Delta w_1$ and $\Delta w_2$ are the rotation angles of stick $OA$ and stick $OC$, respectively.

The shear strain and stress were calculated from $\Delta a$ and $\Delta\alpha_2$ as follows:

$$\varepsilon_{12} = \frac{1}{2}\left(\frac{a\Delta\alpha_2 + \Delta a\sin(\frac{\alpha_1}{2})}{a\left(1+\cos(\frac{\alpha_1}{2})\right)} + \frac{2\Delta a\cos(\frac{\alpha_1}{2})}{2a\sin(\frac{\alpha_1}{2})}\right) \tag{16}$$

$$\sigma_{12} = \frac{\tau}{d} = \frac{2\beta D\left(1-\exp(-\beta\Delta a)\right)\exp(-\beta\Delta a)}{ad\left(1+\cos(\frac{\alpha_1}{2})\right)} \tag{17}$$

The in-plane shear modulus of graphene block defined by $\mu_{12}^{gb} = \sigma_{12}/(2\varepsilon_{12})$ was determined using $\varepsilon_{12} = 0.1\%$.

*In conclusion.* The numerical results showed that $E_1^{gb} = E_2^{gb} = 1.1511$ TPa, $\mu_{12}^{gb} = 0.4822$ TPa and as a consequence from Eq. (5) $\nu_{12}^{gb} = \nu_{21}^{gb} = 0.1936$.

Moreover, as the following expression $\mu_{12}^{gb} = \dfrac{E_1^{gb}}{2(1+\nu_{12}^{gb})}$ was satisfied, it could be concluded that the graphene block had in-plane isotropic property.

*4.1.4. Out-plane engineering constants*

From the conclusion of the previous section, the graphene block was isotropic in-plane. Therefore, the graphene block could be assumed as a transversely isotropic material which was characterized by 5 engineering constants. Out-plane engineering constants that must be calculated were $E_3^{gb}$, $\mu_{31}^{gb} = \mu_{23}^{gb}$, $\nu_{13}^{gb} = \nu_{23}^{gb}$ and $\nu_{31}^{gb} = \nu_{32}^{gb}$.

For out-of-plane deformation, non-bonding energy played a major role in the total potential energy. The van der Waals force resulting from the interaction between a carbon atom on a sheet of graphene and all the atoms in an adjacent graphene sheet could be expressed as follows [13]:

$$U_{vdW} = 4ur_0^6\left[r_0^6 S_{12} - S_6\right], \tag{18}$$

where

$$S_m = \sum_j r_j^{-m} = \sum_j (d^2 + l_j^2)^{-\frac{m}{2}} \tag{19}$$

where, $d$ is the distance between two graphene sheets and $l_j = \sqrt{x_{1,j}^2 + x_{2,j}^2}$ is the radial distance from the considered atom in the graphene sheet to the perpendicular projection onto this graphene sheet of the $j$th atom in the adjacent graphene sheet ($x_{1,j}$ and $x_{2,j}$ are the coordinates of the $j$th atom in the graphene sheet).

In this work, the constants $u = 3.825 \times 10^{-3}$ nN Å and $r_0 = 3.432$ Å were based on [42] which were different from Cho *et al.*.

The energy density defined as the energy per unit volume was given by Cho *et al.* [13] as follows (taking into account only the interaction between two adjacent graphene layers):

$$\Phi = \frac{4\,u\,r_0^6}{d\,A}\left[r_0^6\,\bar{S}_{2,12} - \bar{S}_{2,6}\right], \tag{20}$$

where $A = 2.62$ Å$^2$ is the area per atom in a graphene sheet. The quantity $\bar{S}_m$ was the average value of the sum $r^{-m}$ for the two equilibrium positions: one in which the atom was vertically over the center of a hexagon, the other one is in which the atom was above a vertex of a hexagon (see Fig. 11).

The components $C^{gb}_{3333}$ and $C^{gb}_{3131}$ of the fourth-order elasticity tensor of graphene block was derived from the energy density (see Eq. (20)) with respect to $\varepsilon_{33}$ and $\varepsilon_{13}$ respectively [13]:

$$C^{gb}_{3333} = d_0^2\left(\frac{\partial^2\Phi}{\partial d^2}\right)_{d=d_0}, \tag{21}$$

$$C^{gb}_{3131} = d_0^2\left(\frac{\partial^2\Phi}{\partial x_1^2}\right)_{x_1=x_1^0}, \tag{22}$$

where

$$\frac{\partial^2\bar{S}_m}{\partial d^2} = -m\bar{S}_{m+2} + m(m+2)d^2\bar{S}_{m+4}, \tag{23}$$

$$\frac{\partial^2\bar{S}_m}{\partial x_1^2} = -m\bar{S}_{m+2} + m(m+2)\sum_j \frac{x_{1,j}^2}{(d_0^2 + x_{1,j}^2 + x_{2,j}^2)^{(m+4)/2}}, \tag{24}$$

and $d_0$ is the layer spacing and $x_1^0$ is the coordinate on the $x_1$-axis of the atom in the undeformed state.

Then, Poisson's ratio defined by $\nu^{gb}_{13} = -\varepsilon_{33}/\varepsilon_{11}$ was determined by imposing a strain $\varepsilon_{11}$ on the entire graphene sheet. The strain $\varepsilon_{22}$ was obtained from $\nu^{gb}_{12} = -\varepsilon_{22}/\varepsilon_{11}$. The layer spacing $d_z$ after deformation at equilibrium state was obtained through the minimum energy assumption, that is [13]:

$$\frac{\partial\Phi}{\partial d} = \frac{4ur_0^6}{dA}\left[\left(r_0^6\frac{\partial\bar{S}_{12}}{\partial d} - \frac{\partial\bar{S}_6}{\partial d}\right) - \frac{1}{d}\left(r_0^6\bar{S}_{12} - \bar{S}_6\right)\right] = 0, \qquad \text{at } d = d_z. \tag{25}$$

The solution $d_z$ of Eq. (25) which is a nonlinear equation was solved by the Newton-Raphson method. The result was then used to calculate $\varepsilon_{33}$. Poisson's ratio $\nu^{gb}_{13}$ was determined with the imposed strain $\varepsilon_{11} = 0.1\%$.

From $C^{gb}_{3333}, C^{gb}_{3131}, \nu^{gb}_{13}, \nu^{gb}_{12}$ and the known in-plane engineering constants, the quantities $E^{gb}_3$ and $\mu^{gb}_{31}$ were calculated as follows [13]:

$$E^{gb}_3 = \frac{(1-\nu^{gb}_{12})E^{gb}_1 C^{gb}_{3333}}{(1-\nu^{gb}_{12})E^{gb}_1 + 2(\nu^{gb}_{13})^3 C^{gb}_{3333}}, \tag{26}$$

$$\mu^{gb}_{31} = C^{gb}_{3131}. \tag{27}$$

*4.1.5. Elasticity tensor of graphene block with arbitrary layer orientation*

We then determined the elasticity tensor of graphene block with arbitrary layer orientation. As observed experimentally by TEM, the graphene blocks were arranged with any orientation in the chitosan matrix, therefore it was necessary to calculate the elasticity tensor of the graphene block with an arbitrary layer orientation to include in the model. The layer orientation of the graphene block was defined by the unit vector $\mathbf{n} = (n_1, n_2, n_3)$, which was the vector perpendicular to the graphene sheets. First, in the case of $\mathbf{n} = (0, 0, 1)$, because the graphene block was transversely isotropic, the non-zero components of the elasticity tensor of the graphene block could be expressed in

terms of the five independent elastic constants calculated in the previous section ($E_1^{gb}, \nu_{12}^{gb}, E_3^{gb}, \mu_{31}^{gb}$ and $\nu_{31}^{gb}$) [43]:

$$C_{1111}^{gb} = C_{2222}^{gb} = \Lambda + \frac{0.5E_1^{gb}}{1+\nu_{12}^{gb}}, \tag{28}$$

$$C_{1122}^{gb} = \Lambda - \frac{0.5E_1^{gb}}{1+\nu_{12}^{gb}}, \tag{29}$$

$$C_{1133}^{gb} = C_{2233}^{gb} = 2\Lambda\nu_{31}^{gb}, \tag{30}$$

$$C_{3333}^{gb} = E_3^{gb} + 4\Lambda(\nu_{31}^{gb})^2, \tag{31}$$

$$C_{2323}^{gb} = C_{3131}^{gb} = \mu_{31}^{gb}, \tag{32}$$

$$C_{1212}^{gb} = \frac{1}{2}\left(C_{1111}^{gb} - C_{1122}^{gb}\right). \tag{33}$$

with

$$\Lambda = \frac{0.25\, E_3^{gb}}{0.5\left(1-\nu_{12}^{gb}\right)\left(\dfrac{E_3^{gb}}{E_1^{gb}}\right) - (\nu_{31}^{gb})^2}. \tag{34}$$

Next, the fourth-order elasticity tensor for graphene block (a transversely isotropic material) with arbitrary layer orientation, $\mathbf{n} = (n_1, n_2, n_3)$, was expressed as follows [43]:

$$\begin{aligned} C_{ijkl}^{gb} =& \lambda^{gb}\delta_{ij}\delta_{kl} + \mu^{gb}(\delta_{ik}\delta_{jl} + \delta_{il}\delta_{jk}) + \varsigma^{gb}(\delta_{ij}n_k n_l + \delta_{kl}n_i n_j) \\ &+ \varphi^{gb}(\delta_{ik}n_j n_l + \delta_{jk}n_i n_l + \delta_{il}n_j n_k + \delta_{jl}n_i n_k) + \zeta^{gb}n_i n_j n_k n_l, \end{aligned} \tag{35}$$

where $\delta_{ij}$ is Kronecker's symbol, $\lambda^{gb}$, $\mu^{gb}$, $\varsigma^{gb}$, $\varphi^{gb}$ and $\zeta^{gb}$ are five independent constants that characterize the material properties of graphene block. If $\mathbf{n} = (0, 0, 1)$, these five engineering constants are calculated from the components of the elasticity tensor in Eqs. (28)-(32) as follows:

$$\lambda^{gb} = C_{1122}^{gb}, \tag{36}$$

$$\mu^{gb} = \frac{1}{2}(C_{1111}^{gb} - C_{1122}^{gb}), \tag{37}$$

$$\varsigma^{gb} = C_{1133}^{gb} - C_{1122}^{gb}, \tag{38}$$

$$\varphi^{gb} = C_{2323}^{gb} - \frac{1}{2}(C_{1111}^{gb} - C_{1122}^{gb}), \tag{39}$$

$$\zeta^{gb} = C_{1111}^{gb} + C_{3333}^{gb} - 2C_{1133}^{gb} - 4C_{2323}^{gb}. \tag{40}$$

*4.2. Determination of material properties of graphene oxide block at the nanoscale*

In this section, the effective material properties containing graphene oxide blocks with intercalated structure were modeled which was further used at the microscale to describe homogeneous inclusions reinforcing a matrix. Graphene oxide blocks had a laminate structure consisting of alternating graphene oxide and chitosan layers with thickness of 1 nm and 2 nm, respectively. With this type of structure, Milton's method [47] was relevant to determine the effective material properties of a graphene oxide block which was described as a stratified material. Milton's method permitted to obtain the effective elasticity tensor of laminate material with arbitrary layer orientations. This was perfectly adapted to obtain a model in which the stratified inclusions were arbitrarily oriented in a matrix.

The following introduced the method principle for calculating the effective elasticity tensor of a two-phase laminate material. In a laminate domain $\Omega$ consisting of two phases, the linear elasticity equations (by neglecting body forces) of each phase were given as follows:

$$\begin{cases} \boldsymbol{\sigma} = \mathbb{C}\,\boldsymbol{\varepsilon}, \\ \boldsymbol{\varepsilon} = \dfrac{1}{2}\left(\operatorname{grad}\mathbf{u} + (\operatorname{grad}\mathbf{u})^T\right), \\ \operatorname{div}\boldsymbol{\sigma} = \mathbf{0}, \end{cases} \tag{41}$$

consisting of the constitutive relation $(41)_1$, the infinitesimal strain second-order tensor $(41)_2$ and the equations of equilibrium in which the body forces have been neglected $(41)_3$. In these equations, the Cauchy stress second-order

tensor is denoted $\boldsymbol{\sigma}$, $\boldsymbol{\varepsilon}$ is the infinitesimal strain second-order tensor, $\mathbf{u}$ is the displacement vector, $\mathbb{C}$ is the fourth-order elasticity tensor, div is the divergence operator, grad is the gradient operator and the superscript $T$ is the transpose operator.

The key to determining the effective tensors of laminate materials was to seek for solutions to the partial differential equations by assuming that specific components of the fields were constant or, equivalently, that certain projections of the fields were uniform fields. It was assumed that $\boldsymbol{\sigma}, \boldsymbol{\varepsilon}$ and $\mathbb{C}$ only varied in the direction of the layers, characterized by the unit vector $\mathbf{n}$:

$$\boldsymbol{\sigma} = \boldsymbol{\sigma}(y), \quad \mathbb{C} = \mathbb{C}(y), \quad \boldsymbol{\varepsilon} = \boldsymbol{\varepsilon}(y), \quad \text{where } y = \mathbf{x} \cdot \mathbf{n}. \tag{42}$$

For the sake of simplicity, let us consider the case when the vector $\mathbf{n}$ was oriented in the $\mathbf{e}_1$-direction, $\mathbf{n} = (1, 0, 0)$, so $y = x_1$. Components $\sigma_{11}$, $\sigma_{12}$, $\sigma_{31}$, $\varepsilon_{22}$, $\varepsilon_{33}$ and $\varepsilon_{23}$ were constant in the whole domain and the tensors $\boldsymbol{\sigma}$ and $\boldsymbol{\varepsilon}$ were rewritten as follows:

$$\boldsymbol{\sigma} = \begin{pmatrix} \sigma_{11} & \sigma_{12} & \sigma_{31} \\ \sigma_{12} & \sigma_{22}(y) & \sigma_{23}(y) \\ \sigma_{31} & \sigma_{23}(y) & \sigma_{33}(y) \end{pmatrix}, \qquad \boldsymbol{\varepsilon} = \begin{pmatrix} \varepsilon_{11}(y) & \varepsilon_{12}(y) & \varepsilon_{31}(y) \\ \varepsilon_{12}(y) & \varepsilon_{22} & \varepsilon_{23} \\ \varepsilon_{31}(y) & \varepsilon_{23} & \varepsilon_{33} \end{pmatrix}. \tag{43}$$

The two fourth-order tensors $\mathbb{\Gamma}_1(\mathbf{n})$ and $\mathbb{\Gamma}_2(\mathbf{n})$ which were the projections out of the plane and on the plane of normal $\mathbf{n}$. When $\mathbf{n} = (1, 0, 0)$, we had:

$$\mathbb{\Gamma}_1(\mathbf{n})\mathbf{B} = \begin{pmatrix} b_{11} & b_{12} & b_{13} \\ b_{12} & 0 & 0 \\ b_{13} & 0 & 0 \end{pmatrix} \qquad \mathbb{\Gamma}_2(\mathbf{n})\mathbf{B} = \begin{pmatrix} 0 & 0 & 0 \\ 0 & b_{22} & b_{23} \\ 0 & b_{23} & b_{33} \end{pmatrix}, \tag{44}$$

where $b_{ij}$ are the components of arbitrary symmetric second-order tensor $\mathbf{B}$. Because $\mathbb{\Gamma}_1(\mathbf{n})$ and $\mathbb{\Gamma}_2(\mathbf{n})$ are projections onto mutually orthogonal subspaces, the two following properties are satisfied:

$$\mathbb{\Gamma}_i(\mathbf{n})\,\mathbb{\Gamma}_j(\mathbf{n}) = \delta_{ij}\mathbb{\Gamma}_i(\mathbf{n}), \text{for } i, j = 1, 2 \qquad \text{and} \qquad \mathbb{\Gamma}_1(\mathbf{n}) + \mathbb{\Gamma}_2(\mathbf{n}) = \mathbb{I}, \tag{45}$$

where $\delta_{ij}$ is Kronecker's symbol and $\mathbb{I}$ is the fourth-order identity tensor.

From equations (43) and (44) we had:

$$\mathbb{\Gamma}_1(\mathbf{n})\boldsymbol{\sigma} = \mathbb{\Gamma}_1(\mathbf{n})\langle\boldsymbol{\sigma}\rangle_\Omega, \qquad \mathbb{\Gamma}_2(\mathbf{n})\boldsymbol{\varepsilon} = \mathbb{\Gamma}_2(\mathbf{n})\langle\boldsymbol{\varepsilon}\rangle_\Omega, \tag{46}$$

where the symbol $\langle\star\rangle_\Omega$ denotes the volume average of $\star$ over domain $\Omega$.

To find the effective elasticity tensor, the polarization field (second-order tensor) $\mathbf{p}$ was introduced:

$$\mathbf{p}(\mathbf{x}) = (\mathbb{C}(\mathbf{x}) - c_0\mathbb{I})\boldsymbol{\varepsilon}(\mathbf{x}) = \boldsymbol{\sigma}(\mathbf{x}) - c_0\boldsymbol{\varepsilon}(\mathbf{x}), \tag{47}$$

where $c_0$ is an arbitrary constant that can be freely chosen. From Eq. (47), the infinitesimal strain $\boldsymbol{\varepsilon}(\mathbf{x})$ and its average $\langle\boldsymbol{\varepsilon}(\mathbf{x})\rangle_\Omega$ could be expressed in terms of the polarization field $\mathbf{p}$ and its average $\langle\mathbf{p}(\mathbf{x})\rangle_\Omega$:

$$c_0\,\boldsymbol{\varepsilon}(\mathbf{x}) = -\mathbb{M}(\mathbf{x})\,\mathbf{p}(\mathbf{x}), \quad c_0\,\langle\boldsymbol{\varepsilon}(\mathbf{x})\rangle_\Omega = \mathbb{M}^e\,\langle\mathbf{p}(\mathbf{x})\rangle_\Omega, \tag{48}$$

where the following tensors have been introduced:

$$\mathbb{M}(\mathbf{x}) = c_0\,(c_0\,\mathbb{I} - \mathbb{C}(\mathbf{x}))^{-1}, \quad \mathbb{M}^e = c_0\,(c_0\,\mathbb{I} - \mathbb{C}^e)^{-1}, \tag{49}$$

where the superscript $e$ designates the average of the field.

By using Eq. (47), one showed that the average polarization field could be formulated as follows:

$$\langle\mathbf{p}(\mathbf{x})\rangle_\Omega = [\mathbb{M}^e - \mathbb{\Gamma}_1(\mathbf{n})]^{-1}\,\mathbf{v} = \langle[\mathbb{M}(\mathbf{x}) - \mathbb{\Gamma}_1(\mathbf{n})]^{-1}\rangle_\Omega\,\mathbf{v}, \tag{50}$$

for all uniform field $\mathbf{v}$.

Since the relation (50) held for all fields $\mathbf{v}$, this relationship implied the general formula given by:

$$[\mathbb{M}^e - \mathbb{\Gamma}_1(\mathbf{n})]^{-1} = \langle[\mathbb{M}(\mathbf{x}) - \mathbb{\Gamma}_1(\mathbf{n})]^{-1}\rangle_\Omega. \tag{51}$$

With these relations, the calculus of the effective elasticity tensor $\mathbb{C}^e$ was obtained as follows:

1. evaluation of: $\mathbb{L} = \langle[\mathbb{M}(\mathbf{x}) - \mathbb{\Gamma}_1(\mathbf{n})]^{-1}\rangle_\Omega$,

2. from (51), evaluation of: $\mathbb{M}^e = \mathbb{L}^{-1} + \mathbb{\Gamma}_1(\mathbf{n})$,

3. from (49), evaluation of: $\mathbb{C}^e = c_0\,(\mathbb{I} - (\mathbb{M}^e)^{-1})$.

It is noteworthy that the general form of the components of tensors $\mathbb{\Gamma}_1(\mathbf{n})$ and $\mathbb{\Gamma}_2(\mathbf{n})$ were given by:

$$[\mathbb{\Gamma}_1(\mathbf{n})]_{ijkl} = \frac{1}{2}\Big(n_i\delta_{jk}n_l + n_i\delta_{jl}n_k + n_j\delta_{ik}n_l + n_j\delta_{il}n_k\Big) - n_in_jn_kn_l, \tag{52}$$

$$[\mathbb{\Gamma}_2(\mathbf{n})]_{ijkl} = \frac{1}{2}\Big(\delta_{ik}\delta_{jl} + \delta_{il}\delta_{jk}\Big) - [\mathbb{\Gamma}_1(\mathbf{n})]_{ijkl}, \tag{53}$$

where $n_i$, for $i = 1, 3$, designates the $i$th component of the vector $\mathbf{n}$.

*4.3. Asymptotic homogenization procedure for micro- and macroscale*

The asymptotic method is a powerful tool for solving periodic domain problems. The details of the homogenization procedure of this method can be easily found in literature, for example in books of Auriault *et al.* [48] and Mei *et al.* [49]. In this section, the principle and the main results of this method are presented.

We considered a two-phase periodic composite material whose the representative periodic cell was denoted by $Y$ included in the tridimensional space at the microscopic scale. The characteristic length of the periodicity at the microscopic scale was denoted by $\ell_c$ whereas the characteristic length at the macroscopic scale was denoted by $L_c$. To ensure a clear separation between the two scales, it was assumed that $\ell_c/L_c = \epsilon \ll 1$. Domain $Y$ was composed of phases $a$ and $b$, occupying the domains $Y^a$ and $Y^b$, respectively and their interface $\Gamma$:

$$Y = Y^a \cup Y^b, \qquad Y^a \cap Y^b = \emptyset, \qquad \partial Y^a \cup \partial Y^b = \Gamma. \tag{54}$$

*4.3.1. Microscopic scale governing equations*

Let us denote $\boldsymbol{\sigma}^\alpha$, $\boldsymbol{\epsilon}^\alpha$ and $\mathbf{u}^\alpha$ the second-order stress tensor, the second-order infinitesimal strain tensor and the displacement vector, respectively. The quantity $\mathbb{C}^\alpha$ was the fourth-order elasticity tensor. The upper index $\alpha = a, b$ represented the phase $a$ and phase $b$, respectively. Each phase was assumed to be a linear elastic material whose constitutive relation was given by Hooke's law:

$$\boldsymbol{\sigma}^\alpha = \mathbb{C}^\alpha\,\boldsymbol{\epsilon}^\alpha \qquad \text{in } Y^\alpha,\ \alpha = a, b \tag{55}$$

which could be written in components as:

$$\sigma^\alpha_{ij} = C^\alpha_{ijkl}\,\epsilon^\alpha_{kl} \qquad \text{in } Y^\alpha,\ \alpha = a, b \tag{56}$$

where the summation convention over repeated indices was used and the infinitesimal strain tensor was defined by:

$$\boldsymbol{\epsilon}(\mathbf{u}) = \frac{1}{2}\left(\operatorname{grad}\mathbf{u} + (\operatorname{grad}\mathbf{u})^T\right), \tag{57}$$

and these components by:

$$\epsilon^\alpha_{kl}(\mathbf{u}^\alpha) = \frac{1}{2}\left(\frac{\partial u^\alpha_k}{\partial x_l} + \frac{\partial u^\alpha_l}{\partial x_k}\right). \tag{58}$$

The equilibrium equation (by neglecting body forces) and the continuity conditions at the interface $\Gamma$ read:

$$\operatorname{div}\boldsymbol{\sigma}^\alpha = \mathbf{0}, \qquad \text{in } Y^\alpha,\ \alpha = a, b \tag{59}$$

$$\mathbf{u}^a = \mathbf{u}^b \qquad \text{on } \Gamma \tag{60}$$

$$\boldsymbol{\sigma}^a\,\mathbf{n} = \boldsymbol{\sigma}^b\,\mathbf{n} \qquad \text{on } \Gamma \tag{61}$$

where $\mathbf{n}$ is the unit normal vector to the interface $\Gamma$.

*4.3.2. Asymptotic expansions*

As defined above, $l_c$ represented the unit length of the periodicity and $L_c$ represented the length at the macroscale such that the condition $l_c/L_c = \epsilon \ll 1$ might be satisfied. We introduced the fast and slow coordinates $\mathbf{x} = (x_1, x_2, x_3)$ and $\mathbf{y} = \mathbf{x}/\epsilon = (y_1, y_2, y_3)$ for coordinates at the macro and microscale, respectively.

The classical two-scale asymptotic method consisted in expanding the displacement field as a power series of $\epsilon$ in the following form:

$$\mathbf{u}^\alpha(\mathbf{x}) = \mathbf{u}^{\alpha(0)}(\mathbf{x}, \mathbf{y}) + \epsilon\,\mathbf{u}^{\alpha(1)}(\mathbf{x}, \mathbf{y}) + \epsilon^2\,\mathbf{u}^{\alpha(2)}(\mathbf{x}, \mathbf{y}) + ... \tag{62}$$

where the fields $\mathbf{u}^{\alpha(0)}, \mathbf{u}^{\alpha(1)}, \mathbf{u}^{\alpha(2)}$, ... are $Y$-periodic with respect to $\mathbf{y}$. Terms of the order of $\epsilon^n$ were represented by the upper index $(n)$, where macroscale variables were expressed in the order of $\epsilon^0$.

*4.3.3. Cell problem and effective properties*

By substituting Eq. (62) into Eq. (59) at order $\epsilon^{-2}$, Eq. (60) at order $\epsilon^0$ and Eq. (61) at order $\epsilon^{-1}$, we get $\mathbf{u}^{\alpha(0)}$ depended only on the macroscale coordinates, that is, $\mathbf{u}^{\alpha(0)}(\mathbf{x},\mathbf{y}) = \mathbf{U}^{\alpha(0)}(\mathbf{x})$.

According this result and using the periodic conditions that $\mathbf{u}^{\alpha(1)}$ and $\boldsymbol{\sigma}^{\alpha(0)}\,\mathbf{n}$ must satisfy on the boundary of $Y$ where $\mathbf{n}$ denoting the unit outer normal, by linearity, one deduced that $\mathbf{u}^{\alpha(1)}$ could be written in $Y$ as:

$$\mathbf{u}^{\alpha(1)}(\mathbf{x},\mathbf{y}) = \epsilon_{ij}^{\alpha(0)}(\mathbf{x})\,(\boldsymbol{\chi}^{\alpha})^{ij}(\mathbf{y}) + \mathbf{U}^{\alpha(1)}(\mathbf{x}), \tag{63}$$

where the term $\boldsymbol{\epsilon}^{\alpha(0)}(\mathbf{x}) \equiv \boldsymbol{\epsilon}^{\alpha(0)}(\mathbf{U}^{\alpha(0)})$ could be interpreted as a constant eigenstrain within the cell of independent components $\epsilon_{ij}^{\alpha(0)}$. The functions $[\boldsymbol{\chi}^{\alpha}]_k$ are $Y$-periodic with respect to $\mathbf{y}$ and are defined by the components of a third-order tensor $[\boldsymbol{\chi}^{\alpha}]_k \equiv (\chi^{\alpha})_k^{ij}$ which are the solution of the elementary cell problems given by:

$$\frac{\partial}{\partial y_j}\left[C_{ijkl}^{\alpha}\left(\frac{1}{2}\Big(\frac{(\chi^{\alpha})_k^{mn}}{\partial y_l} + \frac{(\chi^{\alpha})_l^{mn}}{\partial y_k}\Big) + \delta_{mk}\delta_{nl}\right)\right] = 0, \quad \text{in } Y^{\alpha},\ \alpha = a,b \tag{64}$$

$$(\chi^{a})_i^{mn} = (\chi^{b})_i^{mn},\ \text{on } \Gamma \tag{65}$$

$$\left[C_{ijkl}^{a}\left(\frac{1}{2}\Big(\frac{(\chi^{a})_k^{mn}}{\partial y_l} + \frac{(\chi^{a})_l^{mn}}{\partial y_k}\Big) + \delta_{mk}\delta_{nl}\right)\right] n_j = \left[C_{ijkl}^{b}\left(\frac{1}{2}\Big(\frac{(\chi^{b})_k^{mn}}{\partial y_l} + \frac{(\chi^{b})_l^{mn}}{\partial y_k}\Big) + \delta_{mk}\delta_{nl}\right)\right] n_j, \text{on } \Gamma \tag{66}$$

$$[\boldsymbol{\chi}]_k \quad \text{are } Y\text{-periodic with respect to } \mathbf{y}, \tag{67}$$

$$\langle(\chi)_i^{mn}\rangle_Y = 0, \tag{68}$$

where $\delta_{ij}$ is the Kronecker symbol and $\langle\star\rangle_Y$ denotes the volume average of $(\star)$ over domain $Y$:

$$\langle\star\rangle_Y = \frac{1}{Y}\left\{\int_{Y^a}(\star)dV + \int_{Y^b}(\star)dV\right\}. \tag{69}$$

At order $\epsilon^0$ of Eq. (59), order $\epsilon^2$ of Eq. (60) and order $\epsilon$ of Eq. (61), the macroscopic equation could be written as:

$$\frac{\partial}{\partial y_j}\langle\sigma_{ij}^{(1)}\rangle_Y = 0, \tag{70}$$

$$\sigma_{ij}^{\alpha(1)} = \frac{1}{2}C_{ijkl}^{\alpha}\Big(\frac{\partial u_k^{\alpha(1)}}{\partial y_l} + \frac{\partial u_l^{\alpha(1)}}{\partial y_k}\Big) + \frac{1}{2}C_{ijkl}^{\alpha}\Big(\frac{\partial u_k^{\alpha(0)}}{\partial x_l} + \frac{\partial u_l^{\alpha(0)}}{\partial x_k}\Big). \tag{71}$$

Therefore, by combining the results of the cell problem, Eqs. (64)-(68), the effective elastic coefficients were given by the fourth-order tensor $\mathbb{C}^e$ whose the components were determined as follows:

$$C_{ijkl}^{e} = \langle C_{ijmn}\Big(\frac{1}{2}\Big(\frac{(\chi)_m^{kl}}{\partial y_n} + \frac{(\chi)_n^{kl}}{\partial y_m}\Big) + \delta_{mk}\delta_{nl}\Big)\rangle_Y. \tag{72}$$

## 5. Results and discussion

*5.1. Numerical implementation*

In this modelling, perfect binding between the inclusions and the polymer matrix was assumed and thermal effects were not included. For the multiscale approach, the problem was solved from small scale to larger scale. The results of the smaller scale were introduced into the next larger scale.

At the nanoscale, the elasticity tensor of inclusions, including the graphene block, monolayer graphene oxide and graphene oxide block, was obtained by explicit formulas (see sections 4.1 and 4.2). To calculate the component values of effective elasticity tensor at the micro- and macroscale from Eq. (72) in the asymptotic approach, we needed to calculate the functions $[\boldsymbol{\chi}^{\alpha}]_k$ of two phases from the cell problem Eqs. (64)-(68). The Comsol Multiphysics software based on the finite element method was used to solve this problem. The following paragraph summarizes the problem-solving process at the micro- and macroscale using the Comsol Multiphysics software.

At the microscale, a process consisting of two processes running concurrently in Matlab and Comsol environments was used to construct random disc inclusions and apply different effective mechanical properties to the respective inclusions. These two processes are described in detail below.

The geometrical construction of disc-shaped inclusions randomly placed in a given volume domain was carried out by using a method proposed elsewhere [50]. This method, which was previously introduced for discs-shaped in 2D and spheres-shaped in 3D [51], used an algorithm based on molecular dynamics. In this algorithm, all particles (inclusions) were randomly created with a null volume into a cube of a given side. A random velocity vector was assigned at each particle. The particles were then set in motion and each volume gradually increased from zero. Two types of incidents were checked at each iteration: binary collisions and collisions between particles and the cell faces. When a binary collision occurred, with respect to the kinetic energy conservation principle, the velocities of the two concerned particles were updated. Nevertheless, if a particle left the volume domain through a face, it must appear from the opposite side to carry out the periodicity conditions. The simulation stopped when the imposed volume fraction was reached. This algorithm was more efficient than the random sequential adsorption algorithm introduced in [52, 53], in particular, since it could generate very dense packings in a short computation time.

The principal steps of the algorithm are summarized hereafter.

(i) $N$ ellipsoids were randomly created into a cube domain of side $L$. The volume of each ellipsoid was initially null. At each ellipsoid, a random velocity, an angular velocity, and a random orientation were attributed.

(ii) The growth rates of the semi-principal axes $a_0, b_0, c_0$ of ellipsoid were chosen such that $b_0 = a_0/r_1$ and $c_0 = a_0/r_2$, where $r_1$ and $r_2$ denotes respectively the two aspect ratios that are input in the algorithm.

(iii) The elliptical particles were then put in translational and rotational motion and their volumes gradually increased. At each step, two types of collisions were checked and computed: binary collision between two ellipsoids and collision between a particle and a cube domain face. If the first type of collision occurred, the velocity and angular velocity of the involved particles were updated. However, if an ellipsoid intersected a cube domain face, its periodic image was created on the opposite side.

(iv) The algorithm stopped when the volume fraction $\phi$ was reached.

(v) The ellipsoid was then completely replaced by discs by keeping their position, orientation, aspect ratio, and volume. The model was then returned to the actual size with the reference of the thickness of the graphene sheet.

(vi) Finally, a visual check was performed to check the presence of overlaps among the inclusions or between the inclusions and the RVE surface.

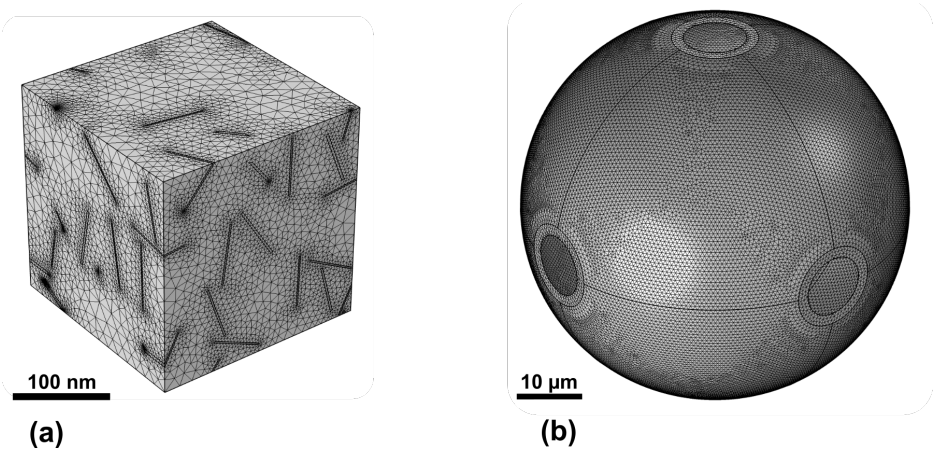


Figure 14: Example of a meshed specimen of (a) a RVE at the microscale with 2% graphene volume fraction and 40 inclusions and (b) a representative unit cell at macroscale with a porosity of 98.24%.

For the finite element method (FEM), an unstructured mesh of tetrahedral finite elements with quadratic Lagrange interpolating polynomials was used. Two types of mesh sizes were specified for inclusions and matrices. More precisely, the maximum element size of the inclusion was 5 nm, and the maximum element size of the matrix

was $L/5$, of which $L$ was the size of the RVE. The MUltifrontal Massively Parallel sparse direct Solver (MUMPS) method with the relative tolerance of 0.001 was used to solve the final linear system. An example of a meshed specimen of a RVE at the microscale with inclusions was the graphene blocks, as shown in Fig. 14(a).

At the macroscale, to construct the unit cell with the desired porosity, we changed the surface thickness of the hollow sphere. Here, the effective mechanical properties obtained from the results of the microscale were introduced like those of the solid phase. Subsequently, the procedure for solving the cell problem to calculate the functions $[\boldsymbol{\chi}^{\alpha}]_k$ for the solid phase, and then obtaining the effective elasticity tensor, was conducted using the same method as that used at the microscale (see section 4.3). For meshing, the element maximal size of the unit cell was taken to be $2t_s$ where $t_s$ is the surface thickness of the hollow sphere. Figure 14b presents an example of a meshed specimen of representative unit cell at the macroscale with a porosity of 98.24%, which corresponds to a surface thickness of 1.24 $\mu$m.

The effective elasticity tensor $C^e_{ijkl}$ could be expressed as the elasticity matrix $\hat{\mathbf{C}}^e$ using Kelvin notation (see Appendix A). In the following, for the sake of brevity, the exponent $\blacksquare^e$ referring to the effective properties was dropped where $\blacksquare$ is the computational quantity. Instead, the exponents $\blacksquare^{(1)}$, $\blacksquare^{(2)}$ and $\blacksquare^{(3)}$ characterize computational quantities at the nano-, micro-, and macroscales, respectively.

### *5.2. Effective mechanical properties of inclusions at the nanoscale*

In this section, we discuss the effective mechanical properties of inclusions including the graphene block, monolayer graphene oxide and graphene oxide block. Additionally, we briefly compare our findings for the mechanical properties of graphene blocks with the results obtained by Cho *et al.* [13].

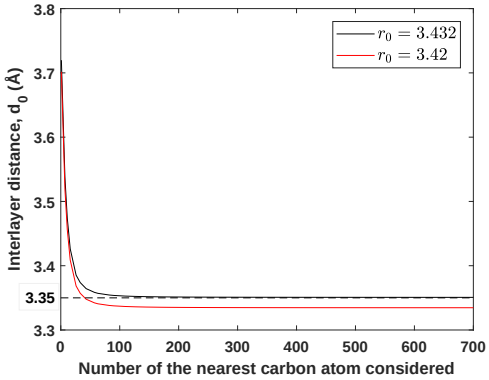


Figure 15: Influence of the number of carbon atoms considered on the value of layer spacing $d_0$.

First, to confirm the relevance of using Kelly and Duff's constants [42] instead of Girifalco and Lad's [41], we recalculated the layer spacing $d_0$ of graphene block in no load condition. In particular, $d_0$ was determined based on Eq. (25) under stress and strain-free conditions, and the influence of the number of carbon atoms considered (the number of nearest carbon atoms contributing to the sum $S_m$) on the value of $d_0$ was also investigated. The results presented in Fig. 15 showed that the interlayer distance $d_0$ reached an asymptote with 300 atoms in both cases which showed the converged solutions with respect to the number of carbon atoms. Therefore, at least of 300 carbon atoms will be included in the graphene blocks. Using Kelly and Duff's constant ($r_0 = 3.432$ Å) and Girifalco and Lad's constant ($r_0 = 3.42$ Å) gave convergent values of $d_0$ of 3.35 Å and 3.33 Å, respectively. The results coincided in the case of Kelly and Duff's constant with the known value of $d_0 = 3.35$ Å, showing that this constant is more compatible with the method used to calculate the effective mechanical properties of the graphene block. Next, we compared the results obtained for the effective mechanical properties of graphene block with those from the work of Cho *et al.* [13]. Because graphene block (or graphite) had transverse isotropic properties, the in-plane engineering constants $E_1^{(1)}$, $\nu_{12}^{(1)}$, and out-of-plane engineering constants $E_3^{(1)}$, $\mu_{13}^{(1)}$, $\nu_{13}^{(1)}$ were presented (see Tab. 2). It could be seen that the results obtained are not significantly different from those of Cho *et al.* [13]. However, the modification of the engineering constants reinforced the validity of the molecular-mechanical method used to calculate the effective mechanical properties of graphene block.

In addition, the non-zero components of the effective elasticity tensor of the three inclusion types, including graphene block, graphene oxide monolayer, and graphene oxide block, are also presented in Tab. 3 using Kelvin notation. Here, the three types of inclusions all had the same orientation vector $\mathbf{n} = (0, 0, 1)$. The results confirmed that the graphene block and graphene oxide block had transverse isotropic properties, while the graphene oxide

Table 2: Comparison of effective engineering constants of graphene block with the results of Cho *et al.* [13].

| Engineering constants | This work | Cho *et al.* [13] |
|---|---|---|
| $E_1^{(1)}$ (TPa) | 1.151 | 1.153 |
| $\nu_{12}^{(1)}$ | 0.194 | 0.195 |
| $E_3^{(1)}$ (GPa) | 39.932 | 39.511 |
| $\mu_{13}^{(1)}$ (GPa) | 0.268 | 0.268 |
| $\nu_{13}^{(1)}$ | 0.006 | 0.006 |

Table 3: Non-zero components of effective elasticity tensor of graphene block, monolayer graphene oxide and graphene oxide block using Kelvin notation.

| Components of $\hat{\mathbf{C}}^{(1)}$ (GPa) | Graphene block | Monolayer graphene oxide | Graphene oxide block |
|---|---|---|---|
| $\hat{C}_{11}^{(1)}$ | 1196.02 | 520.29 | 188.63 |
| $\hat{C}_{22}^{(1)}$ | 1196.02 | 520.29 | 188.63 |
| $\hat{C}_{33}^{(1)}$ | 39.93 | 520.29 | 1.22 |
| $\hat{C}_{44}^{(1)}$ | 0.54 | 392.65 | 0.41 |
| $\hat{C}_{55}^{(1)}$ | 0.54 | 392.65 | 0.41 |
| $\hat{C}_{66}^{(1)}$ | 963.99 | 392.65 | 151.17 |
| $\hat{C}_{12}^{(1)}$ | 232.03 | 127.64 | 37.46 |
| $\hat{C}_{13}^{(1)}$ | 0.30 | 127.64 | 0.61 |
| $\hat{C}_{23}^{(1)}$ | 0.30 | 127.64 | 0.61 |

monolayer was considered as an isotropic material. It was easy to see that graphene oxide block had the lowest hardness of the three types, predicting the lowest ability to strengthen the hardness of aerogels. Graphene oxide monolayer had an in-plane elasticity that was about half lower than that of graphene block, but it was many times stronger than graphene block in the out-of-plane direction ($\mathbf{e}_3$-direction). The reinforcing ability of these three inclusions for hybrid aerogel elasticity will be discussed in the following section.

### *5.3. Validation of the random generation of inclusions at the microscale*

As discussed, the geometry at the microscale consisted of randomly arranged inclusions in the matrix. With complex geometry, it was necessary to check the validity of the used model. To do so, we begun by looking at the resulting variation of the non-zero components of the effective elasticity matrix at 5 independent computations for the aggregate structure (graphene block) with different graphene volume fractions $f_v = 1\%$ and $f_v = 2\%$. Specifically, we performed the calculation 5 times separately while keeping all input parameters unchanged (for instance, type of inclusion, volume fraction of inclusion, number of inclusions, ...). Here, the RVE size could contain an initial selection of 20 inclusions. As shown in Fig. 16(a)-(b), the non-zero components of the effective elasticity matrix did not change significantly for both graphene volume fractions. It could be observed that $\hat{C}_{11}^{(2)}, \hat{C}_{22}^{(2)}$ and $\hat{C}_{33}^{(2)}$ had a variability larger than of the other components. Their maximum standard deviation was only 1.2% and 2.2% for the graphene volume fractions $f_v = 1\%$ and $f_v = 2\%$, respectively. This suggested that at higher concentrations of inclusions, a larger size of RVE was required, in other words, more inclusions are required in RVE. It could be concluded that the RVE size with the number of inclusions of 20 satisfied the convergence condition of the results for the case of $f_v = 1\%$, which was lower than the result proposed elsewhere [54] (which is 30 inclusions). The reason was that the aspect ratio of the inclusions also affected the sensitivity of the RVE size [55]. Accordingly, increasing the aspect ratio of inclusions increased the dependence of the finite element result on the size of the RVE. The aspect ratio used in this work is 40, which was lower than the aspect ratio of 100 [54], which required a smaller RVE size.

Besides, the isotropy of the material at the microscale could be detected by checking $\hat{C}_{11}^{(2)} = \hat{C}_{44}^{(2)} + \hat{C}_{12}^{(2)}$. The isotropic properties of the material were caused by the random and uniform distribution of inclusions in the polymer matrix. This also helped to prove that the algorithm that generated random inclusions was valid. For that reason, the effective mechanical properties of composites (microscale) could be represented by two quantities Young's modulus and Poisson's ratio to serve as input parameters for the solid phase at the macroscale model. To derive Young's modulus and Poisson's ratio of composites from the effective elasticity matrix $\hat{\mathbf{C}}^{(2)}$, the simple

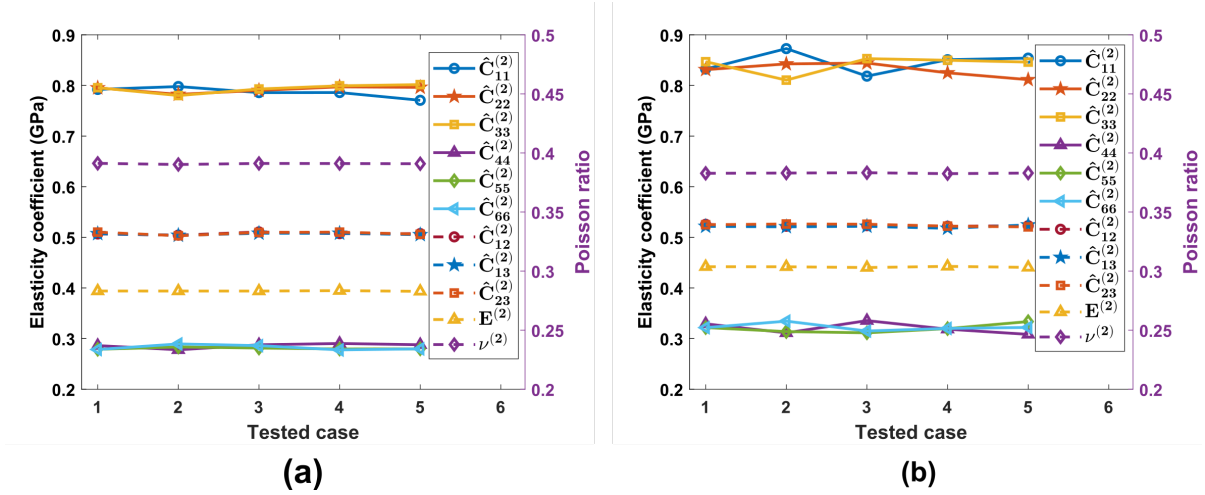


Figure 16: Variation of the non-zero components of the effective elasticity matrix for different configurations of aggregate structure (graphene block) at the microscale with (a) $f_v = 1\%$ and (b) $f_v = 2\%$ of graphene volume fraction. The RVE sizes were built with 20 inclusions.

method of replacing an anisotropic material with the nearest isotropic material was used [56]. Accordingly, the equivalent Lamé constants $\lambda^{(2)}$ and $\mu^{(2)}$ of the composite areogels were calculated from the elasticity matrix $\hat{\mathbf{C}}^{(2)}$ by the following expression:

$$\lambda^{(2)} = \frac{1}{15}\left[\hat{C}^{(2)}_{11} + \hat{C}^{(2)}_{22} + \hat{C}^{(2)}_{33} + 4(\hat{C}^{(2)}_{12} + \hat{C}^{(2)}_{13} + \hat{C}^{(2)}_{23}) - (\hat{C}^{(2)}_{44} + \hat{C}^{(2)}_{55} + \hat{C}^{(2)}_{66})\right], \tag{73}$$

$$\mu^{(2)} = \frac{1}{30}\left[2(\hat{C}^{(2)}_{11} + \hat{C}^{(2)}_{22} + \hat{C}^{(2)}_{33}) - 2(\hat{C}^{(2)}_{12} + \hat{C}^{(2)}_{13} + \hat{C}^{(2)}_{23}) + 3(\hat{C}^{(2)}_{44} + \hat{C}^{(2)}_{55} + \hat{C}^{(2)}_{66})\right]. \tag{74}$$

The Young's modulus and the Poisson's ratio were calculated from Lamé constants $\lambda^{(2)}$ and $\mu^{(2)}$ by the relationships:

$$E^{(2)} = \frac{\mu^{(2)}(3\lambda^{(2)} + 2\mu^{(2)})}{\lambda^{(2)} + \mu^{(2)}}, \qquad \nu^{(2)} = \frac{\lambda^{(2)}}{2(\lambda^{(2)} + \mu^{(2)})}. \tag{75}$$

The graphs of Young's modulus and Poisson's ratio are displayed in Fig. 16, showing that both of these quantities accurately characterized the isotropy of the material at the microscale with a maximum standard deviation of 0.1% and 0.2% for the graphene volume fractions $f_v = 1\%$ and $f_v = 2\%$, respectively. In the following, the number of inclusions in the RVE will be used from 30 to 50 corresponding to the percentage of inclusion volume from 1 to 3%.

### *5.4. Effective mechanical properties of aerogels at the macroscale*

#### *5.4.1. Identification of mechanical properties and experimental validation*

In this section, the identification of mechanical properties and experimental validation were carried out in two steps. In the first step, Young's modulus of the aerogels was identified, while in the second step, the model was validated with experimental results including the experimental data given by Takeshita *et al.* [57] and our compression test results for chitosan aerogel.

Indeed, the identification of mechanical properties and model validation were performed by comparing with experimental results in two aspects including both the relationships between porosity, on the one hand, graphene content, and on the other hand, Young's modulus of aerogels. Specifically in the first step, in order to minimize the number of parameters that could affect the effective mechanical properties of the aerogels, we investigated Young's modulus of the pristine chitosan aerogel ($f_v = 0\%$) as a function of porosity, including different investigated values of the modulus of chitosan $E_{CS}$. In addition, Poisson's ratio of chitosan was fixed at 0.4, *i.e.* $\nu_{CS} = 0.4$. The obtained numerical results were compared with the experimental results to identify the appropriate value of $E_{CS}$ in order to be used in subsequent studies. The results of the model using two values $E_{CS} = 0.35$ GPa and $E_{CS} = 2.5$ GPa with porosity range of $86 - 99\%$ and the experimental results including the experimental data given by Takeshita *et al.* [57] are shown in Fig. 17.

Based on left side of Fig. 17, one could see the non-linearity between Young's modulus and porosity in experimental results when porosity was lower than 94%. The value $E_{CS} = 2.5$ GPa allowed for characterizing aerogel

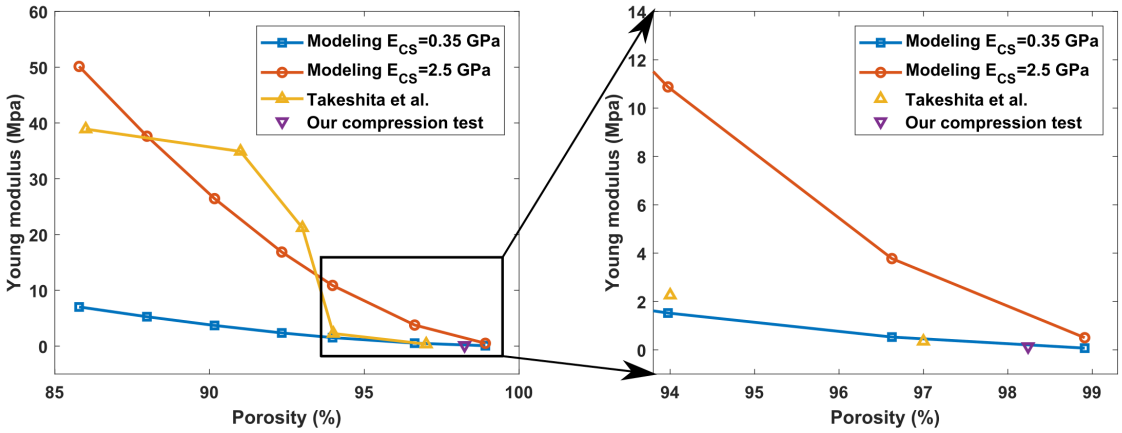


Figure 17: Numerical predictions of Young's modulus of chitosan aerogel compared to the experimental data from Takeshita *et al.* [57] and our compression test results of chitosan aerogel.

mechanical properties over a wide range of porosity ($85 - 99\%$). However, the difference between the numerical results and the experimental results was still quite large at some values of porosity due to the non-linearity stated above. In fact, research in literature is often directed towards the development of ultra-high porosity aerogels with porosity up to 99.8%. Indeed, aerogels possess unique properties arising from their super-porosity, making possible to adapt them for a wide range of applications by adjusting varied factors. These factors include the molecular weight, deacetylation degree as well as aerogel preparation conditions such as the type of acid solvent used in processing, the concentration of the chitosan solution, and the incorporation of additional nanofillers or crosslinking agents [58, 59]. Moreover, the obtained porosity of our aerogels was higher than 98% in all instances. Therefore, we were interested in the porosity values higher than $\geq 94\%$ (see Fig. 17 on the right). It was easy to see that the 0.35 GPa value for Young's modulus of chitosan gave numerical results that matched the experimental results. Therefore, the value $E_{CS} = 0.35$ GPa will be used in the following studies.

In the second step, after selecting a chitosan Young modulus value of $E_{CS} = 0.35$ GPa, the model that was used to estimate the effective mechanical properties of the hybrid graphene-chitosan aerogels was confirmed by comparison with the uniaxial compression tests on aerogel samples with different graphene contents. Since the freezing method used in the preparation of the material was isotropic, the samples were compressed in one direction to determine Young's modulus assuming that the material was isotropic [10]. The uniaxial compression test was performed using a universal testing machine at room temperature (Instron 5567, Boston, Massachusetts, America). The sample was cylindrical in shape with a diameter of 30 mm and a height of 20 mm. Cylindrical samples are subjected to a vertical compression test with a speed of 1 mm/min as shown in Fig. 18(a). Young's modulus was calculated as the ratio between stress and strain in the elastic domain. For each aerogel, the compression test was performed on three samples, and the results were averaged. The experimental results are shown in Fig. 18(b). For comparison purposes, the results obtained through the model for graphene block inclusion as described in the previous sections are also presented in Fig. 18.

The two models included in the comparison were the model $\phi_a = 98.24\%$ and model $\phi_a$ modified. In particular, the first one used a constant porosity value ($\phi_a = 98.24\%$) for all aerogels, while the second one used variable porosity corresponding to different graphene contents present in the aerogel, as calculated in Tab. 1 (see section 3.3). It could be seen that both models gave results quite close to the experimental results, supporting the validity of the used model. As explained, the porosity of the aerogels did not change significantly at low graphene content ($f_w$ ranges from 0% to 5%), the value of 98.24% porosity was averaged by porosity of the aerogels at this graphene content, so the results of the two models were coincident. However, when the graphene content increased, in particular in the case of $f_w = 10\%$, model $\phi_a = 98.24\%$ underestimated Young's modulus of the aerogel compared with experimental results. Indeed, at the high graphene content, which led to a significant decrease in the aerogel porosity, specifically from 98.24% to 98.08%. For this reason, the model $\phi_a$ modified gave the overall results closer to the experimental results than the first model. From this, it could also be inferred that graphene enhanced the mechanical strength of chitosan-based aerogels not only by enhancing the elasticity of the solid phase but also through changing the porosity of the aerogels. Besides, our model was only built up to a graphene content of 10% (corresponding to graphene volume fraction $f_v \approx 6\%$) for an inclusion aspect ratio of 40. This was because our model generated inclusions that were randomly distributed in the polymer matrix to ensure that the inclusions did not overlap,

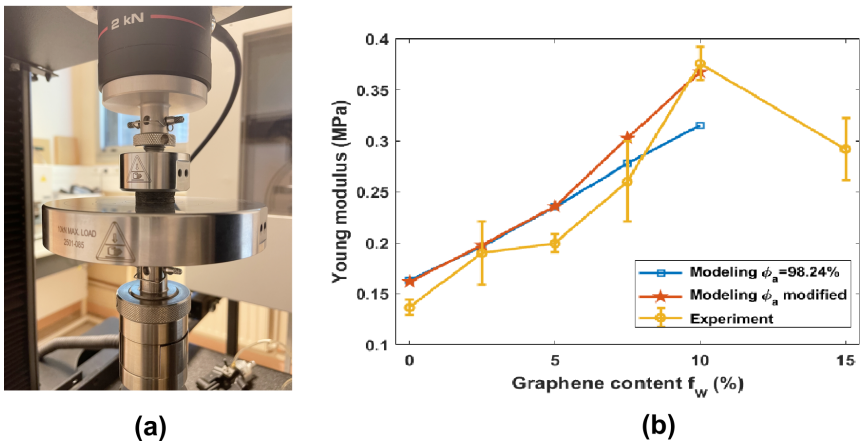


Figure 18: (a) Uniaxial compression test of graphene-chitosan aerogel using Instron 5567 and (b) numerical results with the model $\phi_a = 98.24\%$ and model $\phi_a$ modified compared to the experimental results.

but due to their large aspect ratio, they tended to align in an almost parallel arrangement when the content was too high. Therefore, the model had difficulty building random inclusions at a too large a concentration, which was consistent with the work of Hbaieb *et al.* [54]. This information helped us to explain that the strength of aerogels at the mass percent graphene of 15% was reduced compared with the mass percent graphene of 10% in the experimental results. When the graphene content was too high (larger than 10% by weight), the graphene sheets became more difficult to disperse in the chitosan matrix, and they tended to remain sticked together in parallel to form large agglomerates. These agglomerates weakened the mechanical properties of the aerogels because they hindered the fluidity of the matrix, reducing the bond between the reinforcement and the matrix. This result was also experimentally confirmed in previous works [60, 61]. These results showed that the investigation of the influence of graphene's microstructural parameters on the effective mechanical properties of the aerogels should be carried out in the range $0-5\%$ of the graphene weight fraction $f_w$ (corresponding to the range $0-3\%$ of graphene volume fraction $f_v$) with the aim of eliminating possible effects of porosity.

*5.4.2. Effect of porosity*

In order to consider the material symmetry, an example for the result of the effective elasticity matrix of the chitosan aerogel with the porosity of 98.24%, $E_{CS} = 0.35$ GPa and $\nu_{CS} = 0.4$ was shown below:

$$\hat{\mathbf{C}}^{(3)} = \begin{pmatrix} 2.35 & 0.41 & 0.41 & 0 & 0 & 0 \\ 0.41 & 2.35 & 0.41 & 0 & 0 & 0 \\ 0.41 & 0.41 & 2.35 & 0 & 0 & 0 \\ 0 & 0 & 0 & 6.66 & 0 & 0 \\ 0 & 0 & 0 & 0 & 6.66 & 0 \\ 0 & 0 & 0 & 0 & 0 & 6.66 \end{pmatrix} \text{(MPa)}. \tag{76}$$

This result showed that the elasticity tensor contained three non-zero independent components and had a cubic material symmetry which was characterized by the equalities:

$$\hat{C}_{11} = \hat{C}_{22} = \hat{C}_{33}, \tag{77}$$
$$\hat{C}_{12} = \hat{C}_{13} = \hat{C}_{23}, \tag{78}$$
$$\hat{C}_{44} = \hat{C}_{55} = \hat{C}_{66}. \tag{79}$$

These equalities reflected three mutually orthogonal planes of reflection symmetry plus 90° (degrees) rotation symmetry with respect to these planes.

Therefore, the three engineering constants $E^{(3)}, \mu^{(3)}$ and $\nu^{(3)}$ characterized the effective mechanical properties of aerogels at the macroscale. To study the effect of porosity on the mechanical properties of aerogels, their porosity was varied from $86-99\%$ by changing the wall thickness of the hollow spherical unit cell. The results of three engineering constants $E^{(3)}, \mu^{(3)}$ and $\nu^{(3)}$ are shown in Fig. 19. It is noteworthy that all three engineering constants decreased sharply as the aerogel porosity increased. Specifically, when porosity increased from 86% to

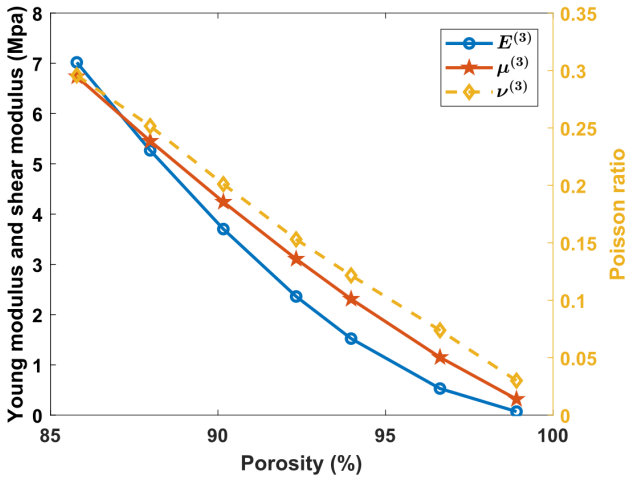


Figure 19: Effect of porosity on the mechanical properties of aerogel.

99%, $E^{(3)}, \mu^{(3)}$ and $\nu^{(3)}$ decreased by 99.0%, 95.3% and 89.8%, respectively. This showed that porosity greatly affected the mechanical strength of the aerogels. Besides, the relationship between $\nu^{(3)}$ and $\mu^{(3)}$ with porosity was close to a linear relationship. This relationship was slightly nonlinear for Young's modulus, $E^{(3)}$ decreasing more strongly in the small porosity range than in the larger porosity range. Interestingly, Young's modulus $E^{(3)}$ was smaller than the shear modulus $\mu^{(3)}$ when the porosity was larger than 87%, whereas most materials typically had Young's modulus higher than the shear modulus. With regard to porosity, we could control porosity by controlling the polymer concentration in solution. Thus, by increasing the initial amount of polymer in the solution, the porosity of the resulting aerogel decreased. From this result, it could be concluded that porosity had an important influence on the mechanical behavior of aerogels, reducing porosity enhanced the mechanical strength. However, it should be noted that the reduction of porosity could lead to an increase in the density, thus a decrease in the thermal and sound insulation of the aerogel [62, 63]. Therefore, the control of porosity needs to be taken into account in the fabrication of aerogels depending on the targeted applications.

*5.4.3. Effect of aspect ratio of inclusions*

In this section, the influence of aspect ratio $r_a$ of inclusions at the microscale varying in the range of $8-65$ on the effective mechanical properties of aerogels for the aggregate structure of graphene was investigated. Figure 20(a) presents the variation of Young's modulus with respect to the aspect ratio of graphene block in 4 cases of the graphene volume fraction given by the values 0.5%, 1%, 1.5% and 2%. The results showed that Young's modulus increased as the aspect ratio increased, with a more pronounced increase observed at higher graphene volume fraction. In addition, Fig. 20(b) shows a near-linear relationship of all three engineering constants (Young's modulus, shear modulus and Poisson's ratio) with respect to the aspect ratio of inclusion at 2% graphene volume fraction. As the aspect ratio increased, Young's modulus and shear modulus both increased, while Poisson's ratio decreased. However, it could be seen that the change in magnitude is different between these three engineering constants. Specifically, when the aspect ratio increased from 8 to 65, Young's modulus increased by 35.5% (corresponding to 0.06 MPa), and shear modulus increased more with 38.6% (corresponding to 0.22 MPa), while Poisson's ratio was almost unchanged (only decreased from 0.043 to 0.042). The results showed interesting mechanical behavior of aerogels as a function of aspect ratio, and also showed the potential of inclusions at high aspect ratio in reinforcing polymer-based aerogels. These results were in good agreement with some previous numerical results from the literature [55, 19]. In fact, the aspect ratio of graphene or graphene oxide could be controlled through ultrasonic treatment or preparation method of graphene oxide [29, 30, 64]. Therefore, this result guided the selection or synthesis of graphene or graphene oxide sheets to achieve high mechanical strength aerogels.

*5.4.4. Effect of microstructural morphology*

In this section, the influence of type-related structural parameters, such as the aggregate structure of graphene, the exfoliated structure of graphene oxide and the intercalated structure of graphene oxide on the macromechanical properties of aerogels, was examined. Figure 21 shows Young's modulus, the shear modulus and Poisson's ratio of aerogels as a function of graphene volume fraction in different inclusion types.

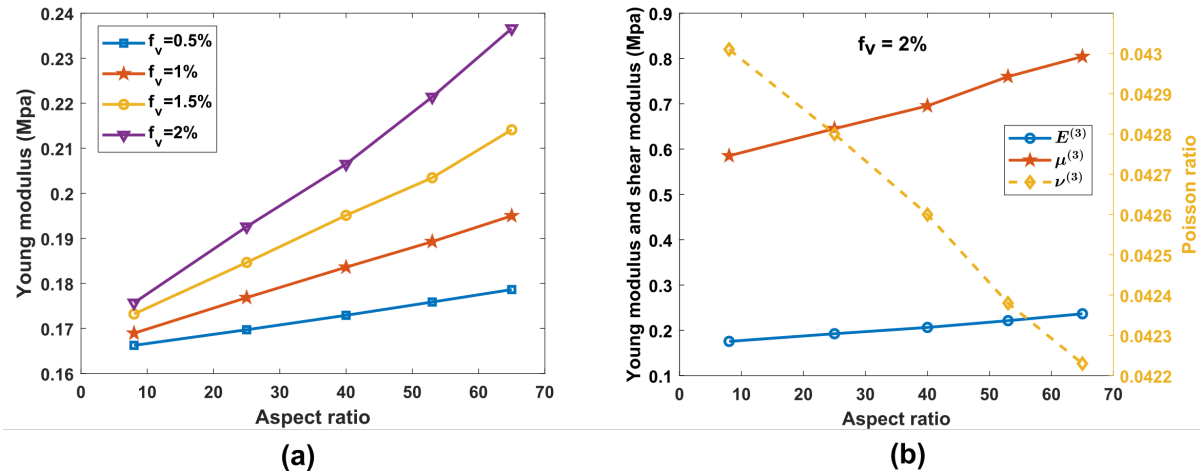


Figure 20: Effect of aspect ratio of inclusion on (a) Young's modulus at different graphene volume fractions, and (b) Young's modulus, shear modulus and Poisson's ratio at 2% graphene volume fraction.

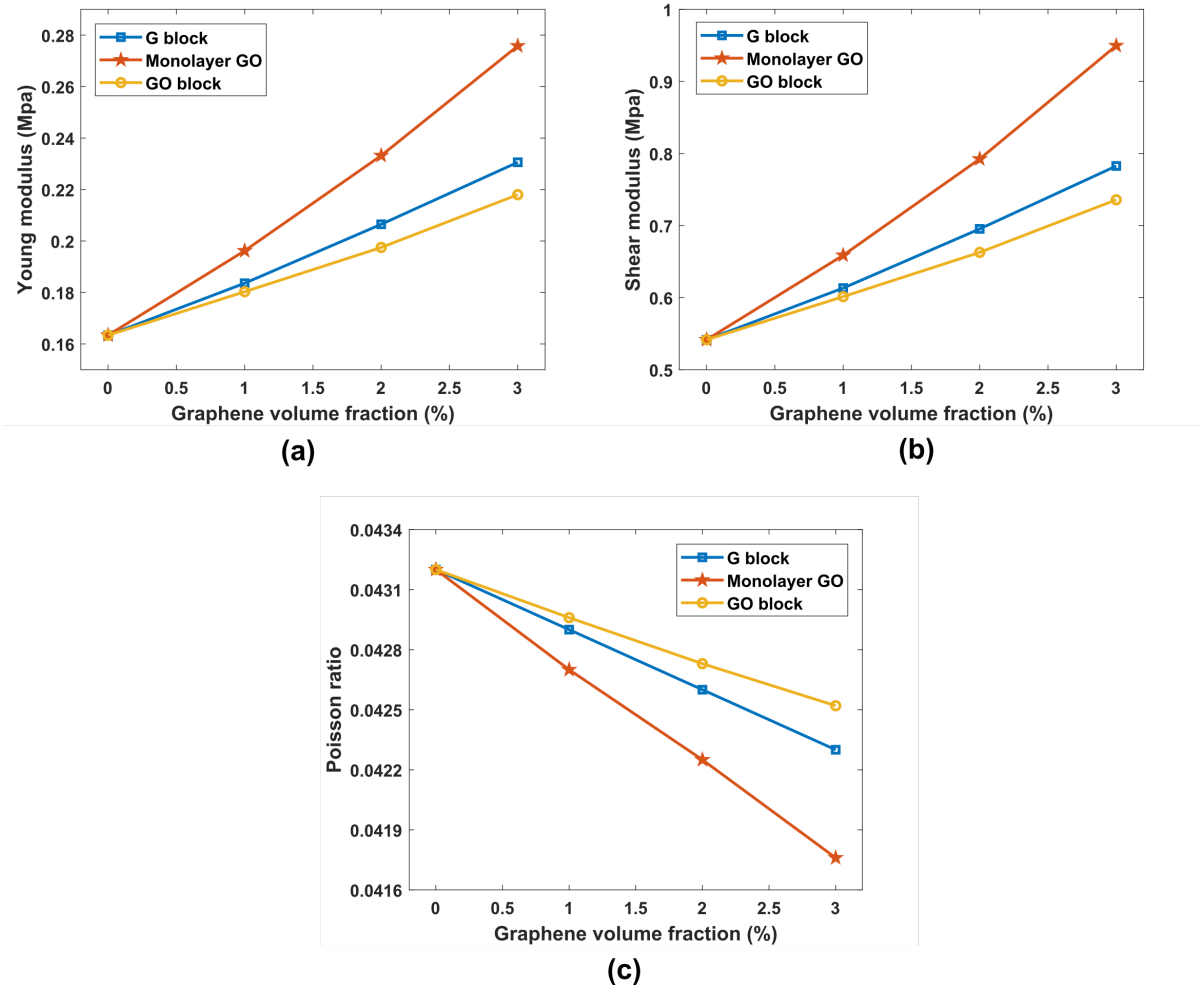


Figure 21: Effect of the inclusion type-related structural parameter on (a) Young's modulus $E^{(3)}$, (b) shear modulus $\mu^{(3)}$ and (c) Poisson's ratio $\nu^{(3)}$.

It could be seen that Young's modulus and the shear modulus increased while Poisson's ratio decreased in all three inclusion types. Although graphene oxide had a Young's modulus lower than half that of graphene, thanks to its intercalated structure, graphene oxide improved the mechanical properties of the aerogels more effectively than graphene. This effect became significantly more important as the reinforcement content increased. The reason was that when graphene existed as aggregates, the interaction between adjacent graphene sheets was based on weak Van der Waals interactions, resulting in much weaker out-of-plane mechanical properties than the in-plane ones (as discussed in section 3.1). On the other hand, the stacking of graphene sheets to form aggregates directly reduced the aspect ratio of inclusions, thus also increasing the elasticity of the aerogel. Therefore, it was understandable that the intercalated structure of graphene oxide had the lowest mechanical strength when it possessed both weak elasticity and low aspect ratio of inclusions simultaneously. Through this study, it could be concluded that when graphene and graphene oxide had the same lateral dimensions, which could occur when synthesized from the same graphite source, graphene oxide with an exfoliated structure provided superior reinforcement of polymer-based aerogels compared to graphene. Therefore, the attempt to oxidize graphene to enhance its dispersibility in the polymer with the aim of creating a exfoliated structure has yielded the expected results. It should be added that the preparation of exfoliated graphene oxide sheets was significantly more cost-effective than exfoliated graphene sheets, therefore graphene oxide was the preferred choice for mechanical reinforcement of polymer-based aerogels.

## 6. Conclusion

This work focused on the numerical and experimental characterizations of the effective mechanical properties associated with composite aerogels based on graphene and chitosan. Such aerogels were synthesized through an environmentally friendly freeze-drying method by directly replacing the liquid phase in the wet gel by the gas phase through sublimation. The effective mechanical properties of materials were obtained by using the multiscale approach. More specifically, the geometrical configurations at different scales were built based on the experimental results. Three types of inclusions were studied namely graphene block, graphene oxide monolayer and graphene oxide block at the nanoscale, then, the positions and orientations of these inclusions were randomly generated in the chitosan matrix at the microscale, and finally, a hollow spherical unit cell was used to describe the macroscopic behavior of the material. In addition, molecular mechanics and Milton's method were used to calculate the effective mechanical properties of graphene block and graphene oxide block type inclusions at the nanoscale, respectively; the method of asymptotic homogenization was applied to study the mechanical behavior of materials at the micro- and macroscales. Following the determination of effective mechanical properties by the homogenization method, a compression test on cylindrical samples of graphene-chitosan aerogels with different graphene contents was also carried out to compare with numerical results. Based on the results of the parametric study, the present paper showed that the aerogels had higher mechanical elasticity as their porosity decreased, which could be achieved by increasing the polymer concentration in the initial solution in the material manufacturing process. However, as discussed, excessive porosity reduction could be detrimental to the characteristic properties of aerogels such as ultra-lightness, excellent thermal insulation and sound insulation properties. Therefore, there is a need for establishing a balance between mechanical elasticity and other properties of aerogels for a specific application.

Concerning the influence of the aspect ratio of inclusions, this paper demonstrated that inclusions with large aspect ratio gave aerogels with improved properties, suggesting for the selection or synthesis of graphene or graphene oxide sheets. Regarding the strengthening ability of graphene and graphene oxide to the mechanical strength of polymer-based aerogels, the results indicated that graphene oxide in the exfoliated state had a better strengthening capacity than graphene in the aggregated state. In contrast, graphene oxide in the intercalated structure gave the weakest reinforcement out of the three inclusion types investigated. This implied that the attempt to improve the effect of graphene on the mechanical properties of polymer-based aerogels by oxidizing the graphene sheets should be achieved when the graphene oxide sheets are completely exfoliated in the polymer matrix. This is possible as graphene oxide has a much higher dispersibility than graphene thanks to its surface functions and is demonstrated by experimental results in previous works where the exfoliated structure of graphene oxide sheets was obtained [65, 22]. Therefore, exfoliated graphene oxide sheets with low cost and high reinforcement efficiency are preferred for mechanical reinforcement of polymer-based aerogels.

Besides, the comparison with experimental results not only confirmed the validity of the model, but also provided more information about the mechanism of aerogel elasticity strengthening in presence of graphene. Specifically, this paper showed that adding graphene to the chitosan matrix on the one hand enhanced the elasticity of the solid phase thanks to the excellent mechanical properties of graphene, thereby improving the aerogel elasticity. On the other hand, reducing the porosity of the aerogel (at high graphene content) led to an increase in the aerogel elasticity. However, the results also showed that increasing the graphene content too much reduced its dispersibility, leading to a decrease in the mechanical strength of aerogels.

The multiscale approach focusing on the ideal disc shape of graphene and the spherical shape of the pore showed to be useful in the material development stage to obtain an initial estimate of the mechanical properties of the studied materials. The relationships between microstructure and effective mechanical properties of materials established from numerical studies provided suggestions for improving the mechanical strength of materials. Nonetheless, taking into account the imperfections in the two-dimensional structure of graphene related to the out-of-plane folds may provide further insights into the effects of graphene on the effective properties of materials based on polymers [66]. In addition, studies on the influence of pore shape including isotropic and anisotropic pores or of uneven arrangement of pores will also be the subject of a further study.

## Appendix A. Kelvin notation

It is noteworthy that to apply projections $\mathbb{\Gamma}_1(\mathbf{n})$ and $\mathbb{\Gamma}_2(\mathbf{n})$ to the second-order symmetric tensors of stress and strain $\boldsymbol{\sigma}$ and $\boldsymbol{\varepsilon}$, these two tensors should be treated in the identical way. Therefore, the Kelvin notation was used in this work, that is:

$$\hat{\boldsymbol{\sigma}} = \begin{pmatrix} \hat{\sigma}_1 \\ \hat{\sigma}_2 \\ \hat{\sigma}_3 \\ \hat{\sigma}_4 \\ \hat{\sigma}_5 \\ \hat{\sigma}_6 \end{pmatrix} = \begin{pmatrix} \sigma_{11} \\ \sigma_{22} \\ \sigma_{33} \\ \sqrt{2}\sigma_{23} \\ \sqrt{2}\sigma_{31} \\ \sqrt{2}\sigma_{12} \end{pmatrix}, \qquad \hat{\boldsymbol{\varepsilon}} = \begin{pmatrix} \hat{\varepsilon}_1 \\ \hat{\varepsilon}_2 \\ \hat{\varepsilon}_3 \\ \hat{\varepsilon}_4 \\ \hat{\varepsilon}_5 \\ \hat{\varepsilon}_6 \end{pmatrix} = \begin{pmatrix} \varepsilon_{11} \\ \varepsilon_{22} \\ \varepsilon_{33} \\ \sqrt{2}\varepsilon_{23} \\ \sqrt{2}\varepsilon_{31} \\ \sqrt{2}\varepsilon_{12} \end{pmatrix},$$

and the stiffness matrix:

$$\hat{\mathbf{C}} = \begin{pmatrix} \hat{C}_{11} & \hat{C}_{12} & \hat{C}_{13} & \hat{C}_{14} & \hat{C}_{15} & \hat{C}_{16} \\ \hat{C}_{12} & \hat{C}_{22} & \hat{C}_{23} & \hat{C}_{24} & \hat{C}_{25} & \hat{C}_{26} \\ \hat{C}_{13} & \hat{C}_{23} & \hat{C}_{33} & \hat{C}_{34} & \hat{C}_{35} & \hat{C}_{36} \\ \hat{C}_{14} & \hat{C}_{24} & \hat{C}_{34} & \hat{C}_{44} & \hat{C}_{45} & \hat{C}_{46} \\ \hat{C}_{15} & \hat{C}_{25} & \hat{C}_{35} & \hat{C}_{45} & \hat{C}_{55} & \hat{C}_{56} \\ \hat{C}_{16} & \hat{C}_{26} & \hat{C}_{36} & \hat{C}_{46} & \hat{C}_{56} & \hat{C}_{66} \end{pmatrix}$$
$$= \begin{pmatrix} C_{1111} & C_{1122} & C_{1133} & \sqrt{2}C_{1123} & \sqrt{2}C_{1113} & \sqrt{2}C_{1112} \\ C_{1122} & C_{2222} & C_{2233} & \sqrt{2}C_{2223} & \sqrt{2}C_{2213} & \sqrt{2}C_{2212} \\ C_{1133} & C_{2233} & C_{3333} & \sqrt{2}C_{3323} & \sqrt{2}C_{3313} & \sqrt{2}C_{3312} \\ \sqrt{2}C_{1123} & \sqrt{2}C_{2223} & \sqrt{2}C_{3323} & 2C_{2323} & 2C_{2313} & 2C_{2312} \\ \sqrt{2}C_{1113} & \sqrt{2}C_{2213} & \sqrt{2}C_{3313} & 2C_{2313} & 2C_{3131} & 2C_{1312} \\ \sqrt{2}C_{1112} & \sqrt{2}C_{2212} & \sqrt{2}C_{3312} & 2C_{2312} & 2C_{2313} & 2C_{1212} \end{pmatrix}.$$

## Declaration of Competing Interest

The authors declare that they have no known competing financial interests or personal relationships that could have appeared to influence the work reported in this paper.

## Data availability

The raw/processed data required to reproduce these findings cannot be shared at this time as the data also forms part of an ongoing study.


## Acknowledgements

This work has benefited from a French government grant managed by ANR within the frame of the national program of Investments for the Future ANR-11-LABX-0022-01 (LabEx MMCD project).

## References


[1] M. Hasan, R. Sangashetty, A. Esther, S. Patil, B. Sherikar, A. Dey, Prospect of thermal insulation by silica aerogel: a brief review, Journal of The Institution of Engineers (India): Series D 98 (2017) 297–304.

[2] S. Sonu, R. Nisha, C. Indu, Multifunctional aerogels: A comprehensive review on types, synthesis and applications of aerogels, Journal of Sol-Gel Science and Technology 105 (2) (2023) 1573–4846.

[3] Z. Liu, Y. Ran, J. Xi, J. Wang, Polymeric hybrid aerogels and their biomedical applications, Soft Matter 16 (2020) 9160–9175.

[4] Y. Li, C. Guo, R. Shi, H. Zhang, L. Gong, L. Dai, Chitosan/nanofibrillated cellulose aerogel with highly oriented microchannel structure for rapid removal of pb (ii) ions from aqueous solution, Carbohydrate polymers 223 (2019) 115048.

[5] G. Meng, H. Peng, J. Wu, Y. Wang, H. Wang, Z. Liu, X. Guo, Fabrication of superhydrophobic cellulose/chitosan composite aerogel for oil/water separation, Fibers and Polymers 18 (4) (2017) 706–712.

[6] S. Alwin, X. Sahaya Shajan, Aerogels: promising nanostructured materials for energy conversion and storage applications, Materials for Renewable and Sustainable Energy 9 (7) (2020) 1–27.

[7] C. Jiménez-Gómez, J. Cecilia, Chitosan: a natural biopolymer with a wide and varied range of applications, Molecules 25 (17) (2020) 3981.

[8] M. Gawryla, E. Arndt, M. Sánchez-Soto, D. Schiraldi, Poly (amide-imide) aerogel materials produced via an ice templating process, Materials 11 (2) (2018) 233.

[9] C. Simón-Herrero, S. Caminero-Huertas, A. Romero, J. Valverde, L. Sánchez-Silva, Effects of freeze-drying conditions on aerogel properties, Journal of Materials Science 51 (2016) 8977–8985.

[10] X. Ge, Y. Shan, L. Wu, X. Mu, H. Peng, Y. Jiang, High-strength and morphology-controlled aerogel based on carboxymethyl cellulose and graphene oxide, Carbohydrate polymers 197 (2018) 277–283.

[11] M. de Luna, C. Ascione, C. Santillo, L. Verdolotti, M. Lavorgna, G. Buonocore, R. Castaldo, G. Filippone, H. Xia, L. Ambrosio, Optimization of dye adsorption capacity and mechanical strength of chitosan aerogels through crosslinking strategy and graphene oxide addition, Carbohydrate polymers 211 (2019) 195–203.

[12] J. Wang, R. Pyrz, Prediction of the overall moduli of layered silicate-reinforced nanocomposites Part I: basic theory and formulas, Composites Science and Technology 64 (7-8) (2004) 925–934.

[13] J. Cho, J. Luo, I. Daniel, Mechanical characterization of graphite/epoxy nanocomposites by multi-scale analysis, Composites science and technology 67 (11-12) (2007) 2399–2407.

[14] A. Montazeri, J. Javadpour, A. Khavandi, A. Tcharkhtchi, A. Mohajeri, Mechanical properties of multi-walled carbon nanotube/epoxy composites, Materials & Design 31 (9) (2010) 4202–4208.

[15] K. Anoukou, F. Zaïri, M. Naït-Abdelaziz, A. Zaoui, T. Messager, J.-M. Gloaguen, On the overall elastic moduli of polymer–clay nanocomposite materials using a self-consistent approach. Part I: Theory, Composites Science and Technology 71 (2) (2011) 197–205.

[16] D. Luo, W.-X. Wang, Y. Takao, Effects of the distribution and geometry of carbon nanotubes on the macroscopic stiffness and microscopic stresses of nanocomposites, Composites Science and Technology 67 (14) (2007) 2947–2958.

[17] V. Vo, V.-H. Nguyen, S. Mahouche-Chergui, B. Carbonnier, D. Di Tommaso, S. Naili, From atomistic structure to thermodynamics and mechanical properties of epoxy/clay nanocomposites: Investigation by molecular dynamics simulations, Computational Materials Science 139 (2017) 191–201. doi:https://doi.org/10.1016/j.commatsci.2017.07.024.
URL https://www.sciencedirect.com/science/article/pii/S0927025617303853

[18] V. Vo, V.-H. Nguyen, S. Mahouche-Chergui, B. Carbonnier, S. Naili, Estimation of effective elastic properties of polymer/clay nanocomposites: A parametric study, Composites Part B: Engineering 152 (2018) 139–150. doi:https://doi.org/10.1016/j.compositesb.2018.06.018.
URL https://www.sciencedirect.com/science/article/pii/S135983681734266X

[19] G. Dai, L. Mishnaevsky Jr, Graphene reinforced nanocomposites: 3d simulation of damage and fracture, Computational Materials Science 95 (2014) 684–692.

[20] B. Mortazavi, J. Bardon, S. Ahzi, Interphase effect on the elastic and thermal conductivity response of polymer nanocomposite materials: 3D finite element study, Computational Materials Science 69 (2013) 100–106.

[21] D. Klvana, J. Chaouki, M. Repellin-Lacroix, G. Pajonk, A new method of preparation of aerogel-like materials using a freeze-drying process, Le Journal de Physique Colloques 50 (C4) (1989) C4–29.

[22] J. Jang, M. Kim, H. Jeong, C. Shin, Graphite oxide/poly (methyl methacrylate) nanocomposites prepared by a novel method utilizing macroazoinitiator, Composites Science and Technology 69 (2) (2009) 186–191.

[23] T. Blanton, D. Majumdar, X-ray diffraction characterization of polymer intercalated graphite oxide, Powder Diffraction 27 (2) (2012) 104–107.

[24] C. Vallés, F. Beckert, L. Burk, R. Mülhaupt, R. Young, I. Kinloch, Effect of the c/o ratio in graphene oxide materials on the reinforcement of epoxy-based nanocomposites, Journal of Polymer Science Part B: Polymer Physics 54 (2) (2016) 281–291.

[25] S. Wang, J. Pu, D. Chan, B. Cho, K. Loh, Wide memory window in graphene oxide charge storage nodes, Applied Physics Letters 96 (14) (2010) 143109.

[26] C. Wan, M. Frydrych, B. Chen, Strong and bioactive gelatin–graphene oxide nanocomposites, Soft Matter 7 (13) (2011) 6159–6166.

[27] B. Mortazavi, O. Benzerara, H. Meyer, J. Bardon, S. Ahzi, Combined molecular dynamics-finite element multiscale modeling of thermal conduction in graphene epoxy nanocomposites, Carbon 60 (2013) 356–365.

[28] R. Rafiee, A. Eskandariyun, Estimating young's modulus of graphene/polymer composites using stochastic multi-scale modeling, Composites Part B: Engineering 173 (2019) 106842.

[29] V. Shevchenko, S. Polschikov, P. Nedorezova, A. Klyamkina, A. Shchegolikhin, A. Aladyshev, V. Muradyan, In situ polymerized poly (propylene)/graphene nanoplatelets nanocomposites: Dielectric and microwave properties, Polymer 53 (23) (2012) 5330–5335.

[30] S. Polschikov, P. Nedorezova, A. Klyamkina, A. Kovalchuk, A. Aladyshev, A. Shchegolikhin, V. Shevchenko, V. Muradyan, Composite materials of graphene nanoplatelets and polypropylene, prepared by in situ polymerization, Journal of Applied Polymer Science 127 (2) (2013) 904–911.

[31] X. Sun, Z. Liu, K. Welsher, J. Robinson, A. Goodwin, S. Zaric, H. Dai, Nano-graphene oxide for cellular imaging and drug delivery, Nano research 1 (3) (2008) 203–212.

[32] X. Zhang, X. Zhao, T. Xue, F. Yang, W. Fan, T. Liu, Bidirectional anisotropic polyimide/bacterial cellulose aerogels by freeze-drying for super-thermal insulation, Chemical Engineering Journal 385 (2020) 123963.

[33] S. Takeshita, A. Sadeghpour, W. Malfait, A. Konishi, K. Otake, S. Yoda, Formation of nanofibrous structure in biopolymer aerogel during supercritical CO2 processing: The case of chitosan aerogel, Biomacromolecules 20 (5) (2019) 2051–2057.

[34] J. Robertson, Properties of diamond-like carbon, Surface and Coatings Technology 50 (3) (1992) 185–203.

[35] C. Zhan, S. Jana, Shrinkage reduced polyimide-graphene oxide composite aerogel for oil absorption, Microporous and Mesoporous Materials 307 (2020) 110501.

[36] I. Polyzos, M. Bianchi, L. Rizzi, E. Koukaras, J. Parthenios, K. Papagelis, R. Sordan, C. Galiotis, Suspended monolayer graphene under true uniaxial deformation, Nanoscale 7 (30) (2015) 13033–13042.

[37] I. Nikolaou, H. Hallil, V. Conédéra, B. Plano, O. Tamarin, J.-L. Lachaud, D. Talaga, S. Bonhommeau, C. Dejous, D. Rebière, Electro-mechanical properties of inkjet-printed graphene oxide nanosheets, physica status solidi (a) 214 (3) (2017) 1600492.

[38] J. Smith, J. Bumgardner, H. Courtney, M. Smeltzer, W. Haggard, Antibiotic-loaded chitosan film for infection prevention: A preliminary in vitro characterization, Journal of Biomedical Materials Research Part B: Applied Biomaterials 94 (1) (2010) 203–211.

[39] D. Aztatzi-Pluma, E. Castrejn-González, A. Almendarez-Camarillo, J. Alvarado, Y. Durán-Morales, Study of the molecular interactions between functionalized carbon nanotubes and chitosan, The Journal of Physical Chemistry C 120 (4) (2016) 2371–2378. doi:10.1021/acs.jpcc.5b08136.
URL https://pubs.acs.org/doi/10.1021/acs.jpcc.5b08136

[40] N. Mushi, S. Utsel, L. Berglund, Nanostructured biocomposite films of high toughness based on native chitin nanofibers and chitosan, Frontiers in chemistry 2 (2014) 99.

[41] L. Girifalco, R. Lad, Energy of cohesion, compressibility, and the potential energy functions of the graphite system, The Journal of Chemical Physics 25 (4) (1956) 693–697.

[42] B. Kelly, M. Duff, On the validity of Lennard-Jones potentials for the calculation of elastic properties of a graphite crystal, Carbon 8 (1) (1970) 77–83.

[43] J. Aboudi, S. Arnold, B. Bednarcyk, Chapter 2 - Constituent material modeling, in: J. Aboudi, S. Arnold, B. Bednarcyk (Eds.), Micromechanics of Composite Materials, Butterworth-Heinemann, Oxford, 2013, pp. 19–85. doi:https://doi.org/10.1016/B978-0-12-397035-0.00002-1.
URL https://www.sciencedirect.com/science/article/pii/B9780123970350000021

[44] F. Lévy, Intercalated layered materials, Vol. 6, Springer Science & Business Media, 2012.

[45] G. Yang, L. Li, W. Lee, M. Ng, Structure of graphene and its disorders: a review, Science and technology of advanced materials 19 (1) (2018) 613–648.

[46] T. Chang, H. Gao, Size-dependent elastic properties of a single-walled carbon nanotube via a molecular mechanics model, Journal of the Mechanics and Physics of Solids 51 (6) (2003) 1059–1074.

[47] G. Milton, The Theory of Composites, Cambridge Monographs on Applied and Computational Mathematics, Cambridge University Press, 2002, Ch. Laminate materials, p. 159184.

[48] J.-L. Auriault, C. Boutin, C. Geindreau, Homogenization of coupled phenomena in heterogenous media, Hermes Science Publications, 2009.

[49] C. Mei, B. Vernescu, Homogenization methods for multiscale mechanics, World scientific, 2010.

[50] E. Ghossein, M. Lévesque, Random generation of periodic hard ellipsoids based on molecular dynamics: A computationally-efficient algorithm, Journal of Computational Physics 253 (2013) 471–490.

[51] B. Lubachevsky, F. Stillinger, Geometric properties of random disk packings, Journal of Statistical Physics 60 (1990) 561–583.

[52] B. Widom, Random sequential addition of hard spheres to a volume, The Journal of Chemical Physics 44 (10) (2004) 3888–3894.

[53] J. Feder, Random sequential adsorption, Journal of Theoretical Biology 87 (2) (1980) 237–254.

[54] K. Hbaieb, Q. Wang, Y. Chia, B. Cotterell, Modelling stiffness of polymer/clay nanocomposites, Polymer 48 (3) (2007) 901–909.

[55] B. Mortazavi, M. Baniassadi, J. Bardon, S. Ahzi, Modeling of two-phase random composite materials by finite element, Mori-Tanaka and strong contrast methods, Composites Part B: Engineering 45 (1) (2013) 1117–1125.

[56] A. Norris, The isotropic material closest to a given anisotropic material, Journal of Mechanics of Materials and Structures 1 (2) (2006) 223–238.

[57] S. Takeshita, S. Yoda, Chitosan aerogels: transparent, flexible thermal insulators, Chemistry of Materials 27 (22) (2015) 7569–7572.

[58] W. Fan, X. Zhang, Y. Zhang, Y. Zhang, T. Liu, Lightweight, strong, and super-thermal insulating polyimide composite aerogels under high temperature, Composites Science and Technology 173 (2019) 47–52.

[59] C. Jiao, J. Xiong, J. Tao, S. Xu, D. Zhang, H. Lin, Y. Chen, Sodium alginate/graphene oxide aerogel with enhanced strength–toughness and its heavy metal adsorption study, International journal of biological macromolecules 83 (2016) 133–141.

[60] K. Chu, C. Jia, Enhanced strength in bulk graphene–copper composites, physica status solidi (a) 211 (1) (2014) 184–190.

[61] M. Kumar, C. Selvan, P. Sampath, K. Raja, R. Nair, Enhanced mechanical properties of glass fiber/epoxy composites using nanoclay, in: 2019 Advances in Science and Engineering Technology International Conferences (ASET), IEEE, 2019, pp. 1–9.

[62] S.-N. Hong, C.-J. Yu, U.-S. Hwang, C.-H. Kim, B.-H. Ri, Effect of porosity and temperature on thermal conductivity of jennite: A molecular dynamics study, Materials Chemistry and Physics 250 (2020) 123146.

[63] Q.-B. Nguyen, V.-H. Nguyen, C. Perrot, A. Rios de Anda, E. Renard, S. Naili, Multiscale approach to characterize effective mechanical, hydraulic and acoustic properties of a new bio-based porous material, Materials Today Communications 26 (2021) 101938.

[64] Y. Hou, S. Lv, L. Liu, X. Liu, High-quality preparation of graphene oxide via the hummers' method: understanding the roles of the intercalator, oxidant, and graphite particle size, Ceramics International 46 (2) (2020) 2392–2402.

[65] J. Chen, D. Zhao, X. Jin, C. Wang, D. Wang, H. Ge, Modifying glass fibers with graphene oxide: Towards high-performance polymer composites, Composites science and technology 97 (2014) 41–45.

[66] J. Meyer, A. Geim, M. Katsnelson, K. Novoselov, T. Booth, S. Roth, The structure of suspended graphene sheets, Nature 446 (7131) (2007) 60–63.